Journal of Wind Engineering & Industrial Aerodynamics 205 (2020) 104326

Contents lists available at ScienceDirect

Journal of Wind Engineering & Industrial Aerodynamics

journal homepage: www.elsevier.com/locate/jweia

An experimental study on dynamic ice accretion and its effects on the aerodynamic characteristics of stay cables with and without helical fillets

Yihua Peng [a,b], Ramsankar Veerakumar [b], Yang Liu [b], Xuhui He [a,c,d], Hui Hu [b,*]

[a] School of Civil Engineering, Central South University, Changsha, 410075, China
[b] Department of Aerospace Engineering, Iowa State University, Ames, IA 50011-1096, United States
[c] National Engineering Laboratory for High Speed Railway Construction, Changsha, 410075, China
[d] Joint International Research Laboratory of Key Technology for Rail Traffic Safety, Changsha, 410075, China

ARTICLE INFO

Keywords:
Ice accretion on bridge stable cables
Aerodynamic characteristics of iced stay cables
Stay cables with helical fillets
Unsteady aerodynamic force measurements
3-D ice shape scanning
Particle image velocimetry

ABSTRACT

An experimental investigation was conducted to examine the effects of helical fillets on dynamic ice accretion process over the surfaces of bridge stay cables and evaluate its effects on the aerodynamic characteristics of the stay cables under both dry rime and wet glaze icing conditions. The experimental study was performed in the Icing Research Tunnel of Iowa State University (i.e., ISU-IRT). Four bridge stay cable models, including a standard plain cable model and three helical filleted cable models of different helical pitch lengths, were used for the experimental investigation. During the experiment, in addition to using a high-speed imaging system to record the dynamic ice accretion process over the cable surfaces, a Digital Image Projection (DIP) based 3D scanning system was also utilized to quantify the 3D shapes of the ice structures accreted on the test models. While a high-resolution digital Particle Image Velocimetry (PIV) system was used to characterize the wake flows behind the cable models during the ice accreting process, the time variations of the aerodynamic drag forces acting on the test models were also measured by using a pair of force/moment transducers mounted at two ends of the cable models. It was found that, under the rime icing condition, the helical filleted cable models accreted more ice structures than the standard plain cable model. However, the helical filleted cable models were found to have less ice accretion under the wet glaze icing condition. The pitch length of the helical fillets was also found to affect the ice accretion process substantially. Under the rime icing condition, while the aerodynamic drag forces acting on the cable models were found to decrease continuously with more rime ice accreting over the cable surfaces, the drag reduction due to the rime ice accretion was found to be less obvious for the helical filleted cable models, in comparison with that obtained for the standard plain cable model. Under the glaze icing condition, the aerodynamic drag forces acting on the cable models were found to decrease quickly at the initial stage of the glaze icing process, and then increase gradually with the increasing ice accretion time at the later stage of the ice accreting process. PIV flow field measurements were correlated with the force measurement data to elucidate the underlying physics for a better understanding of the variation characteristics of the aerodynamic forces acting on the cable models under different icing conditions.

1. Introduction

Atmospheric icing on structure surfaces has been widely recognized as a severe weather hazard for various engineering applications, including aircraft propellers (Liu et al., 2018, 2019a), aircraft wings (Bragg et al., 2005; Sherif et al., 1997), wind turbines (Gao et al., 2019a, 2019b; Ibrahim et al., 2018) and electrical power lines (Li et al., 2017; Makkonen et al., 2018; Veerakumar et al., 2020; Zdero and Turan, 2010). Since ice accretion can greatly change the outer profiles of the original engineering designs, thereby, affecting the aerodynamic performance of the structures, ice accretion and its effects on bridge stay cables have also attracted increasing attentions in recent years in the bridge engineering community. Gjelstrup et al. (2012) studied the aerodynamic characteristics and instabilities of bridge hangers (i.e., vertical cables) with simulated thin ice accretion. Demartino et al. (2015) performed ice shape estimation and force measurements of vertical and inclined high-density polyethylene (HDPE) cable models under different icing conditions. These previous studies revealed that the mean aerodynamic coefficients

* Corresponding author.
E-mail address: huhui@iastate.edu (H. Hu).

https://doi.org/10.1016/j.jweia.2020.104326
Received 26 February 2020; Received in revised form 25 June 2020; Accepted 25 July 2020

of bridge stay cables would be affected by the ice accretion significantly. Demartino and Ricciardelli (2015, 2017) studied the aerodynamic stability of iced plain stay cables (i.e., without any helical fillets) and suggested that further studies were required to characterize the aerodynamic effects of surface, section and spanwise irregularities of nominally circular cylinders. Koss et al. (2012) experimentally studied ice accretion on circular cylinders at temperatures from −5 °C to −1 °C. Their results showed that different types of ice (i.e., wet glaze and dry rime ice) accretion occurred under different temperatures, and the cylinder diameter influenced the thermodynamic solidification process and the characteristics of the accreted ice. Koss and Lund (2013) and Koss et al. (2013) investigated the influence of icing on the aerodynamics of stay cables using three different full-scale models (i.e., standard plain, helical fillet and pattern-indented) with two different types of ice (wet and dry). Their results showed that the extension of the accreted ice layer would influence the airflow separation, hence, the aerodynamic characteristics of the cables. The standard plain cable was most affected by ice accretion with respect to the sensitivity of the drag to the Reynolds number. Cao et al. (2018) studied the vertical and torsional vibrations of iced stay cable models under different ice thicknesses simulated by making artificial ice structures with foam. They found that the wind-induced response would increase with the increasing thickness of the accreted ice layer.

Some studies were also carried out to predict galloping and vortex-induced vibrations of iced cables. McComber and Paradis (1998) pointed out that galloping cannot be predicted by the Den Hartog criterion (Hartog, 1932) for thin ice accretions. Vertical galloping may possibly happen even in the case of positive Den Hartog criterion. Demartino and Ricciardelli (2015) compared the predicted results of different galloping models, and found that the results of galloping stability obtained by using different galloping models would vary significantly. Górski et al. (2016) studied Strouhal number of wake vortices shedding from bridge cables with ice accretion at low turbulence levels in order to predict the cable responses due to vortex excitations. It was found that Strouhal number of wake vortices shedding from the ice accreted cables would fluctuate in a certain range with the changes of the Reynolds numbers.

It is well known that, due to the low mass, great flexibility, and low damping, bridge cables are prone to wind-induced vibrations, including vortex-induced vibration, rain-wind-induced vibration, dry galloping, ice galloping, and wake galloping (Jafari et al., 2020). Among various types of cable vibrations, due to the frequent occurrence and the large vibration amplitudes (e.g., 2–3 times of the cable diameter), thereby leading to a fatigue failure to the cables' supports (Jafari et al., 2020), rain-wind-induced vibrations of bridge cables have attracted extensive attentions in recent years. Numerous studies have carried out to elucidate the underlying mechanisms of rain-wind-induced vibrations and explore effective strategies to control the vibrations, thereby, reducing the fatigue failures of the cables and bridge structures caused by the cable vibrations (Hikami and Shiraishi, 1988; Hua and Zuo, 2019; Matsumoto et al., 1992; Zuo and Jones, 2010). It was found that rain-wind-induced vibrations of bridge cables were mainly due to the excitation of axial flows in the near wake and the formation of upper water rivulets Jing et al. (2015, 2017).

The strategies to suppress cable vibrations can be generally divided into two categories: active control methods and passive control methods. While active control methods require external energy input to maintain the control effectiveness (Chen et al., 2013), passive control methods depend on making geometric modifications to the structures, such as adding cross ties between the stay cables (Caracoglia and Jones, 2007; Caracoglia and Zuo, 2009; Yamaguchi and Nagahawatta, 1995), installing dampers near the ends of the cables (Chen et al., 2004), passive flow control methods (Chen et al., 2020), and cable surface modifications (Flamand, 1995; Kleissl and Georgakis, 2011; Matsumoto et al., 1998; Miyata et al., 1994; Zdravkovich, 1981). Due to the advantages in low-cost production and simple maintenance, cable surface modification methods (e.g., adding helical fillets) have attracted most attentions in suppressing rain-wind- and vortex-induced cable vibrations. While Jing et al. (2015, 2017) demonstrated that the formation of upper water rivulets would play an important role to excite rain-wind-induced vibration for bridge stay cables, helical fillets have been found to be able to effectively disturb/suppress the formation of the upper water rivulets over the surfaces of stay cables (Ge et al., 2018; Gu and Du, 2005). Adding helical fillets on the outer protective layers (i.e., HDPE) of stay cables has become the most widely used aerodynamic measure to suppress rain-wind-induced vibration of bridge stay cables.

It is well known that, due to ice accretion or existence of helical fillets, the surface roughness characteristics of the bridge cables would be changed. Several previous studies were also conducted to investigate the aerodynamic characteristics and vibrations of roughed bridge cables. Achenbach and Heinecke (1981) and Farell (1981) found that, with the increase of surface roughness, while the minimum Reynolds number at the critical and supercritical regime decreased gradually, and the minimum value of the drag coefficients increased progressively. While the peak in the Strouhal number spectrum was found to reduce with the increasing surface roughness, the critical range of the Reynolds numbers became shorter as the surface roughness increases. While varying the surface roughness was found to have the most effects on critical range, it has no obvious effects on the drag coefficients at the subcritical regime (Buresti, 1981) due to high boundary layer thickness (Demartino and Ricciardelli, 2017). Ribeiro (1991a, 1991b) carried out an experimental investigation on circular cylinders with three roughness types (i.e., sand paper, wire mesh screen and ribs), and found that the aerodynamic characteristics at the supercritical regime could be obtained at lower Reynolds numbers by increasing the surface roughness of the test models. Ma et al. (2019) studied the effects of surface roughness on the aerodynamic forces and vibrations in the critical Reynolds number range, and reported that the surface roughness would significantly affect the aerodynamic forces in the critical Reynolds number range by reducing the range of transitions on boundary layer flows. Güven et al. (1980) measured the wind pressure distributions over the surfaces of cylindrical test models with different surface roughness characteristics. They found that, with the increasing surface roughness, the thickness of the boundary layer flow over the surfaces of the test models would increase gradually, and the flow separation points were found to move further upstream along the cylinder surfaces. Benidir et al. (2015) studied the effects of surface roughness on the wind pressure distributions, aerodynamic coefficients and aerodynamic stability of stay cables. They showed that, the surface roughness will affect the flow pattern around the test model greatly, and then affect the aerodynamic performance of the stay cables. Schewe (1983, 1986) found that, even a small modification on the cable surface can cause a significant change to the flow file around it. Matteoni and Georgakis (2012, 2015) carried out a wind tunnel study on a series of roughed stay cable models. The results showed that small protuberances on the model surfaces will change the positions of the separation points greatly, leading to the change of the flow patterns around the test model. Rocchi and Zasso (2002) and Benidir et al. (2018) studied the flow characteristics around cable models with helical fillets, and found that the helical fillets can lead to a decrease of the correlation of the vortex shedding among different transversal cylinder sections. The opposite pressure regions appeared on the same side of the sheath. Katsuchi et al. (2017) found that the spiral protuberance cable can suppress both rain-wind-induced vibration and dry galloping. Christiansen et al. (2018a, 2018b) studied the aerodynamics of a full-scaled stay cable with helical fillets at relatively high Reynolds numbers (i.e. at Reynolds numbers above the drag crisis range). It was found that, the local flow structures were dominated by the helical fillets, and the local Strouhal number depended on the angular positions of the helical fillets. Shin (1996) found that the ice structures accreted over the surface of a cable model could protrude well out of the boundary layer flow to cause boundary-layer transition.

While a number of previous studies have been conducted to

investigate ice accretion and its effects on the aerodynamic characteristics of stay cables, only very little can be found in literature to consider the effects of helical fillets on the ice accretion over the surfaces of stay cables. Furthermore, most of the previous studies focused mainly on determining the accreted ice shape and the aerodynamic characteristics of the iced cables after a specified icing duration (e.g., 30 or 60 min). The aerodynamic characteristics of stay cables during the dynamic ice accretion process under different icing conditions, which may significantly affect the stability of the stay cables, have not been well studied. In addition, while almost all the previous studies mainly used a cross-sectional tracing method (i.e., recording the ice contour in the planes perpendicular to the cable axis by cutting the ice sections using heated metal plates and drawing the outer contours of the accreted ice layers on cardboard) to estimate profiles of the accreted ice layers (Demartino et al., 2015; Koss et al., 2012). Such a method can only trace a two-dimensional ice profile at certain sections. It is difficult, if not impossible, to obtain the complex three-dimensional shapes of the accreted ice layers, thereby, the volume and mass distributions of the accreted ice structures.

In the present study, a comprehensive experimental investigation is conducted to examine the effects of helical fillets on the dynamic ice accretion process over the surfaces of stay cables and to assess the corresponding aerodynamic characteristics during the ice accreting process. The experimental study is performed in an Icing Research Tunnel at Iowa State University (i.e., ISU-IRT). It should be noted that, by leveraging the same Icing Research Tunnel (i.e., ISU-IRT) to be used in the present study, Veerakumar et al. (2020) conducted an experimental investigation to examine the dynamic ice accretion process and its effects on the aerodynamic characteristics of a cylindrical cable model. However, since the investigation was targeted specifically for high-voltage power transmission cable applications, the cable model used for the experimental study of Veerakumar et al. (2020) was designed to have smooth surface and much smaller cable diameter (i.e., D = 29 mm), in comparison to the helical filleted bridge cable models used in the present study. Liu et al. (2019b) studied the dynamic ice accretion process on bridge cables with different surface modifications (i.e., pattern-indented surface and helical fillets with a fixed helical pitch of 16D, D is cable diameter). It was found that the addition of surface features could dramatically affect the dynamic ice accretion process and the final topology of the ice structures accreted on the cable surfaces.

While helical fillets have been widely used to suppress rain-wind-induced vibration of bridge cables, the helical pitches of the fillets were found to vary substantially on different bridge cables. The effects of the helical pitches of the fillets on the ice accretion process over bridge cables and the resultant aerodynamic characteristics have not been well explored. Furthermore, the variations of the aerodynamic characteristics of the bridge cables during the ice accreting process under different icing conditions have also never been examined. With theses in mind, four bridge cable models, including a standard plain cable model and three helical filleted cable models with different helical pitch lengths (i.e., 16D, 8D, and πD, respectively), are designed for the present experimental study. During the experiment, in addition to using a high-speed imaging system to record the dynamic ice accretion process over the cable surfaces, a Digital Image Projection (DIP) based 3D scanning system is also utilized to quantify the 3D shapes of the ice structures accreted on the test models. While a high-resolution digital Particle Image Velocimetry (PIV) system is used to characterize the wake flows behind the cable models during the ice accreting process, the time variations of the aerodynamic drag forces acting on the test models are also measured by using a pair of force/moment transducers mounted at two ends of the cable models. The PIV flow field measurements were correlated with the measured aerodynamic force data to elucidate the underlying physics for a better understanding of about the underlying icing physics and the resultant aerodynamic characteristics of the helical filleted bridge cables under different icing conditions.

2. Experimental setup and test models

2.1. Icing research tunnel

The experimental study was carried out in the Icing Research Tunnel of Iowa State University (i.e., ISU-IRT). As shown schematically in Fig. 1, ISU-IRT has a transparent test section with 2000 mm in length, 400 mm in width, and 400 mm in height. The maximum wind speed in the test section is 60 m/s, and the minimum airflow temperature inside ISU-IRT is −25 °C. It usually takes about 40–60 min, depending on the ambient temperature of the laboratory, to reach the temperature of −25 °C inside the test section. While a feedback control system along with a refrigeration system was used to control the desired temperature inside ISU-IRT automatically, the temperature fluctuations during the icing experiments were found to be with ±0.5 °C. Based on the measurement results of thermocouples, the temperature distributions inside ISU-IRT test section were found to be quite uniform (i.e., the maximum temperature differences being smaller than 1.0 °C). The liquid water content (LWC) of the airflow inside ISU-IRT can be controlled from 0.1 g/m^3 to 5.0 g/m^3 by adjusting the flow rates of the 8 water spray nozzles installed at the front the test section. The size of the water droplets exhausted from the spray nozzles is controllable, in the range from 10 to 100 μm. In summary, ISU-IRT has been used to simulate various atmospheric icing scenarios from very dry rime to extremely wet glaze ice conditions for icing physics and anti-/de-icing studies of various engineering applications, including aircraft icing (Waldman and Hu, 2016; Liu et al., 2018, 2019a), aero-engine icing and anti-/de-icing (Li et al., 2020), wind turbine icing (Gao et al., 2019a, 2019b), power transmission cable icing (Veerakumar et al., 2020) and bridge cable icing (Liu et al., 2019b).

2.2. Bridge stay cable models

The present study focused on the effects of helical fillets on the ice accretion process over on the surfaces of bridge cables. Due to the much small size of the helical fillets in comparison with cable diameter, full-scale bridge cable models were selected for the present experimental study in order to observe the dynamic ice accretion process around the helical fillets more clearly. Four stay cable models, referred as C#1 to C#4 and shown in Fig. 2, were used in the present study. The diameter of the cable models is 82 mm (i.e., D = 82 mm), which is within the diameter range of the stay cables commonly used in cable stayed bridges. The cable models are made of high-density polyethylene (HDPE), i.e., with the same material as the outer protective layers of most-commonly-used bridge stay cables in practice (Demartino et al., 2015; Kleissl and Georgakis, 2012; Koss and Lund, 2013). Model C#1 is a standard plain cable model without any helical fillets, serving as the reference case of the present study. Model C#2, C#3 and C#4 have are helical filleted cable models with different helical pitch lengths of $P = 16D$, 8D, and πD, respectively. The helical pitch length, P, is defined as the axial length in which a helical fillet first returns to its original relative position (Kleissl, 2013), and D is the diameter of the cable, excluding the thickness of the helical fillets. The helical fillets are wrapped around the cable surface as a double parallel helix, and the connection between the two helical fillets passes through the center of the circle. The cross-section of the helical fillet is 2.5 mm in width and 2.5 mm in height, which is the typical helical fillet geometry used in practice (Christiansen et al., 2018). The pitch angles, α, between the cable axis and the helical fillet for the cable models C#2, C#3 and C#4 are α ≈ 11°, 21°, and 45°, respectively, as shown in Fig. 2(a).

For the helical filleted cable models, the relative positions of the helical fillets with respect to the incoming airflow vary in the longitudinal direction of the cable models. To better describe the position of the helical fillets, the angle between the incoming airflow with respect to the line connecting the two helical fillets is defined as the orientation angle, θ, as shown in Fig. 2(b). Representative cross sections of $\theta = 0°$, 45°, 90° and 135° are selected in the present study to examine the effects of the

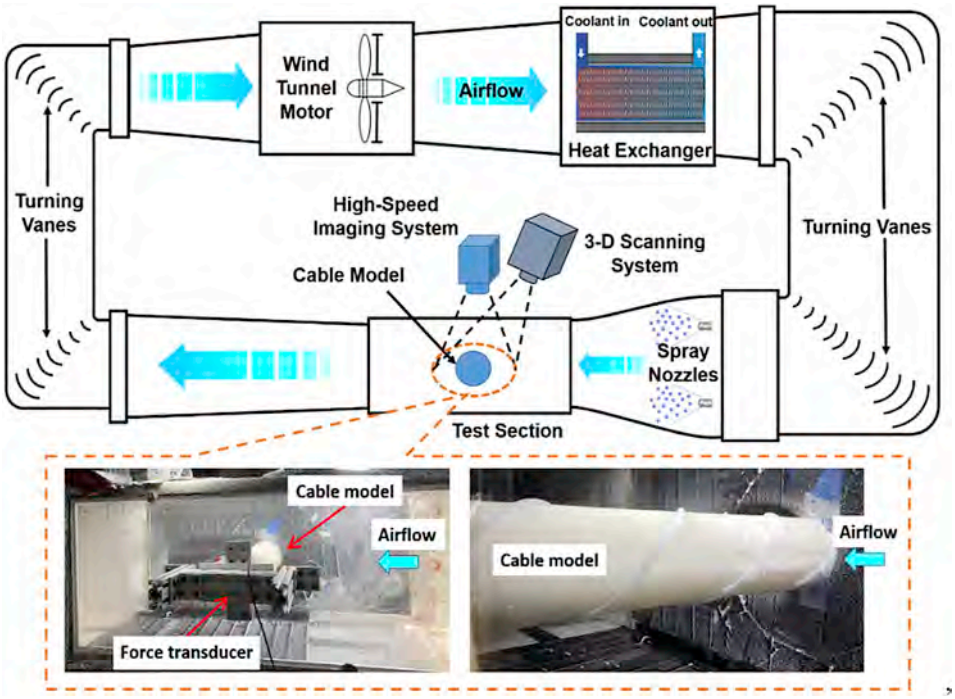

Fig. 1. Schematics of ISU-IRT used in the present study.

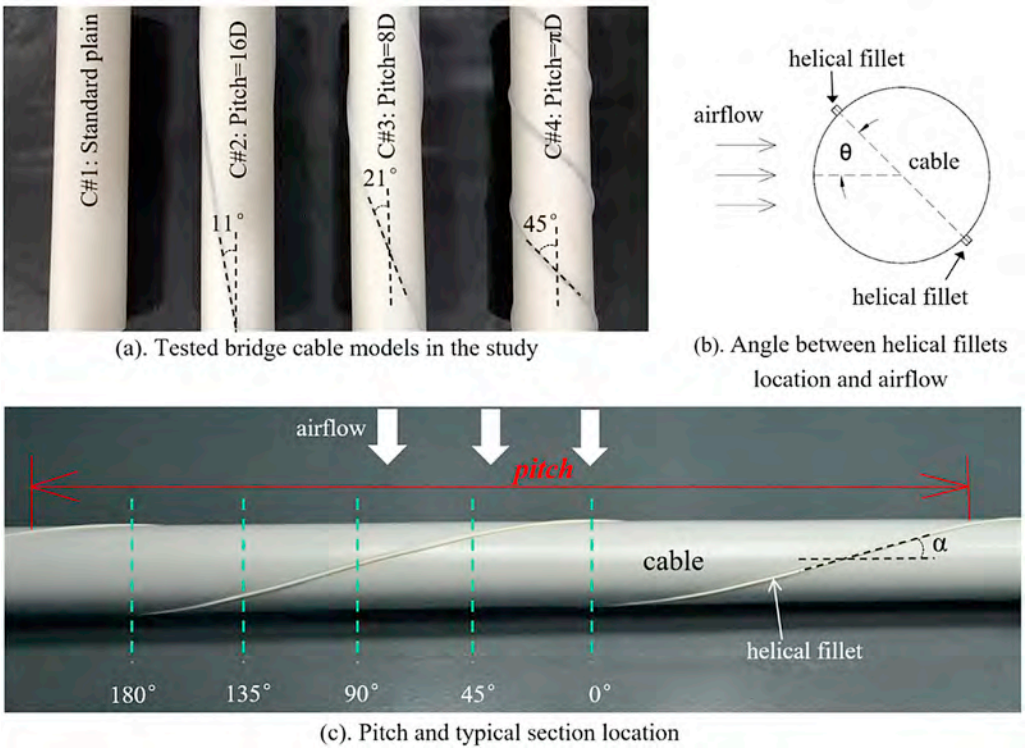

Fig. 2. Tested cable models used in the present study: standard plain cable model C#1; helical fillet cable models C#2 with $P = 16D$; model C#3 with $P = 8D$; and model C#4 with $P = \pi D$.

helical fillets on the ice accretion process, as shown in Fig. 2(c).

2.3. Testing parameters and ice conditions

As described in the previous studies of Hansman and Kirby (1987), Poots (1996), Makkonen and Poots (2000), Naterer (2011), and Liu et al. (2019a), ice accretion over structure surfaces can usually be divided into two categories, i.e., rime ice accretion and glaze ice accretion, depending on the ambient temperatures, wind speed, and liquid water content (LWC) levels in the incoming airflow. Rime ice accretion refers to the scenario at relatively cold ambient temperature (i.e., T_∞<-8.0 °C) and low *LWC* levels, where the airborne, super-cooled water droplets would

be frozen into *ice* almost immediately, upon impinging onto solid surfaces. Glaze ice accretion usually takes place under the conditions with the ambient temperature being relatively high, i.e., just below the water freezing point (i.e., $T_\infty > -8.0\ ^\circ C$), and having relatively high *LWC* levels in the incoming airflow. Upon impinging on a solid surface, only a portion of the impinged water droplets would freeze into ice. The rest of the impacted water mass would stay in liquid at the beginning, run back over the ice-accreting surface, and then froze into ice subsequently at further downstream locations, as driven by the freezing cold boundary layer airflow. While the rime ice usually has an opaque and milk-white appearance with crystalline structures, glaze ice usually has obvious surface water runback and formation of transparent, glassy ice structures, as described in Gao et al. (2019a).

Before conducting the icing experiments, aerodynamic force measurements and three-dimensional scanning of the "clean" cable models (i.e., without any ice accretion over the cable surface) were carried out as the reference case. Table 1 summarizes the testing parameters and icing conditions of the test cases of the present study. For rime icing experiment, the temperature in ISU-IRT was set at $T_\infty = -15.0\ ^\circ C$, and the *LWC* level was set at $LWC = 1.0\ g/m^3$. For the glaze icing experiment, the temperature was at $T_\infty = -5.0\ ^\circ C$, and LWC level was at $LWC = 2.0\ g/m^3$. The free-stream velocity of the incoming airflow was set at $U_\infty = 20.0$ m/s. The corresponding Reynolds number was approximately $Re_D = 1.3 \times 10^5$ for all the cable models. The measurement data included acquired ice accretion images, 3D shapes of the accreted ice structures, the measured aerodynamic force data. The duration of the icing experiment lasted 600 s for each test cases. The three-dimensional (3D) scanning of the accreted ice structures was performed immediately after 600 s of the ice accretion. The airflow fields around the test models were also measured by using a high-resolution digital Particle Image Velocimetry (PIV) system (Gao et al., 2019b; Liu et al., 2019a) to study the changes of the flow characteristics in the wakes behind the cable models induced by the ice accretion process.

2.4. Measurement systems used for the ice accretion experiments

Fig. 3 shows schematically the experimental setup used in the present study. The cable models were mounted horizontally in the middle of the ISU-IRT test section, supported by stainless-steel rods. The gaps between the side walls of ISU-IRT and the ends of the cable models were set to be about 1.50 mm, which is less than 0.5% of the model span length (i.e., $L = 400$ mm), in order to eliminate the effects of the lateral boundary layers and the side walls on the measurement results, as suggested by Barlow et al. (1999). A high-resolution digital imaging system (i.e., PCO Tech, Dimax Camera, 2 K pixels × 2 K pixels in resolution) along with a 60 mm Macrolens (Nikon, 60 mm Nikkor 2.8D) was positioned normal to the cable models to record the dynamic ice accretion process over the surfaces of the test models. For the present study, the spatial resolution of the acquired ice accretion images was ~0.115 mm/pixel. Two sets of high-sensitivity, multi-axis force/moment transducers (i.e., ATI-IA Mini 45) were mounted at two ends of the test models to measure the unsteady aerodynamic forces acting on the cable models (i.e., drag and lift) before and during the dynamic ice accretion process. The precision of the force-moment transducers for force measurements is ±0.25% of the full range (40 N). It should be noted that, since full-scale bridge cable models were used in the present study, the solid blockage ratio of the test models was relatively high, i.e., about 20%. By following the procedures described in Barlow et al. (1999), the effects of the model blockage, the wake interferences and wind tunnel walls on the measurement results were corrected in the present study. With the same Digital Image Projection (DIP)-based 3D scanning system as the one used by Gao et al. (2019c), the 3D shapes of the ice structures accreted over cable models were also measured right after finishing the ice accretion experiments for the four studied cable models.

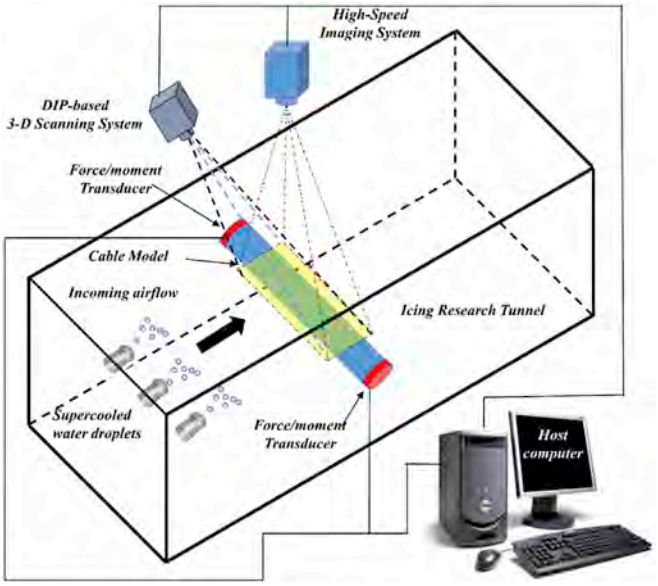

Fig. 3. Experimental setup used for the present study.

A high-resolution digital Particle Image Velocimetry (PIV) system was also used in the present study to quantify the dynamic changes of the wake flows behind the cable models during the dynamic ice accretion process. For the PIV measurements, the airborne super-cooled water droplets in ISU-IRT with the mean volume diameter (MVD) of ~20 μm were used as the tracer particles. The illumination for the PIV measurements was provided by a double-pulsed Nd:YAG laser (i.e., New Wave, Gemini PIV 200) adjusted on the second harmonic and emitting two pulses of 200 mJ at the wavelength of 532 nm with a repetition rate of 10 Hz. The thickness of the laser sheet in the measurement region was set to be about 1.0 mm. A set of convex and concave cylindrical lenses along with optical mirrors were used to generate a laser sheet to illuminate the PIV tracers in the vertical plane passing through the selected sections of the test models. A high-resolution 16-bit digital camera (2 K pixels × 2 K pixels, PCO2000, CookeCorp) was used for PIV image acquisition. The digital camera and the double-pulsed Nd: YAG laser were connected to a workstation (host computer) via a digital delay generator (Berkeley Nucleonics, Model 565), which controlled the timing of the laser illumination and the image acquisition. In the present study, a cinema sequence of over 500 frames of instantaneous PIV image pairs were

Table 1
Test cases in the present study.

Case no.	Cable model	V_∞ [m/s]	T_∞ [°C]	LWC [g/m^3]	Expected ice type	High speed imaging	Force measurement	3D scan	PIV
1	C#1	20	−5.0	2.0	Glaze	0–600 s	0–600 s	at 600 s	Yes
2	C#1	20	−15.0	1.0	Rime	0–600 s	0–600 s	at 600 s	Yes
3	C#2	20	−5.0	2.0	Glaze	0–600 s	0–600 s	at 600 s	–
4	C#2	20	−15.0	1.0	Rime	0–600 s	0–600 s	at 600 s	–
5	C#3	20	−5.0	2.0	Glaze	0–600 s	0–600 s	at 600 s	Yes
6	C#3	20	−15.0	1.0	Rime	0–600 s	0–600 s	at 600 s	Yes
7	C#4	20	−5.0	2.0	Glaze	0–600 s	0–600 s	at 600 s	–
8	C#4	20	−15.0	1.0	Rime	0–600 s	0–600 s	at 600 s	–

obtained to ensure a good convergence of the ensemble-averaged flow statistics based on the PIV measurements. After PIV image acquisition, PIV velocity vectors were obtained by a frame to frame cross-correlation technique with interrogation windows of 32 × 32 pixels and an effective overlap of 50% of the interrogation windows, which result in a spatial resolution of 2.0 mm × 2.0 mm for the PIV measurements. The measurement uncertainty level for the PIV measurement was estimated to be within 2.0%, as described in Chen et al. (2014).

3. Measurement results and discussions

3.1. High-speed imaging results of the dynamic ice accretion processes

Fig. 4 shows typical snapshots of the rime ice accretion processes over the cable models under the typical rime icing condition (i.e., with the incoming airflow velocity $V_\infty = 20$ m/s, $T_\infty = -15$ °C, and $LWC = 1.0$ g/m^3). Due to the very cold ambient temperature and low LWC level, the airborne super-cooled water droplets were found to freeze into ice almost instantly, upon impinging onto the surfaces of the cable models or helical fillets. No obvious water runback was observed on the surfaces of the cable models for all the test cases. In comparison with the standard plain cable model (i.e., the model C#1 without helical fillets), more ice structures were found to accrete over the surfaces of the cable models with helical fillets, along with obvious ice formation/accretion in front of the helical fillets. The ice structures accreted over the surfaces of the cable models were found to be milk-white and opaque in appearance and have rather fine grains, exhibiting typical characteristics of rime ice accretion (Hansman and Kirby, 1987). The ice layers accreted over the front surfaces of the test models were found to become thicker as the ice accretion time increases, as expected. Among the four tested cable models, the model C#4 was found to have the largest amount of ice accretion and roughest surface. After 600 s of the ice accretion experiment, the appearances of the rime ice structures accreted over the front surfaces of the cable models (i.e., within direct impacting region of the super-cooled water droplets) were found to be very similar for all the test cable models, as shown by the dot-and-dash lines in Fig. 4. However, caused by the protrusion of the helical fillets wrapped around the cable surfaces, additional ice accretion structures were also found to accrete along the helical fillets wrapped around the surfaces for the helical filleted cable models. Furthermore, due to the much higher wake turbulence and entrainment of the stronger wake vortices induced by the helical fillets, numerous small-scale, scattered ice structures were also found to form/accrete on the rear surfaces of the helical filleted models C#2, C#3 and C#4. In comparison, the back surface of the plain cable model (i.e., the model C#1 without helical fillets) was found to be rather clean, without any obvious rime ice accretion.

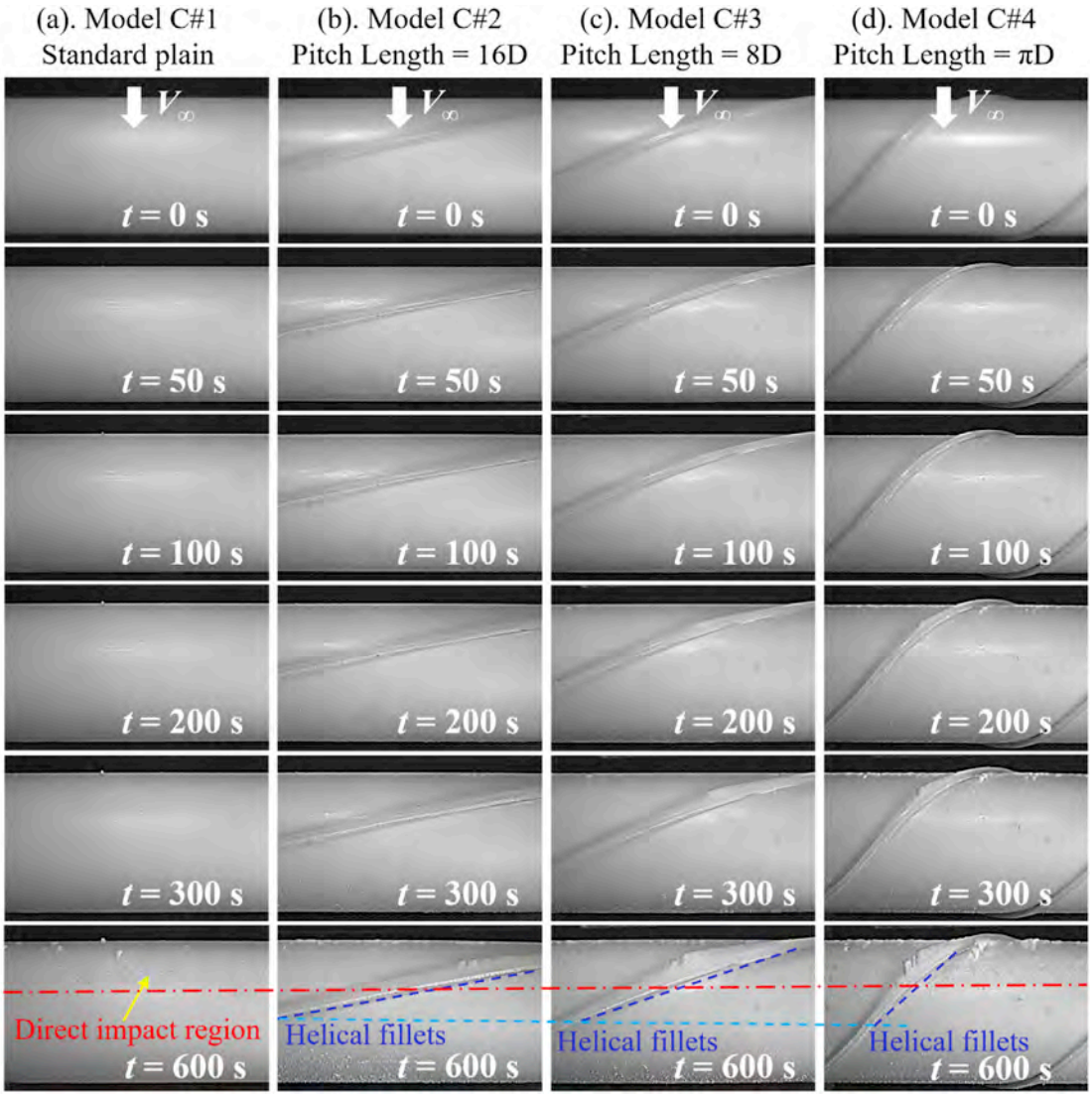

Fig. 4. Typical snapshots of the ice accretion on the cable models under the rime icing condition.

Fig. 5 shows the instantaneous snapshots of the glaze ice accretion on the four cable models under the glaze icing condition with the incoming airflow velocity $V_\infty = 20$ m/s, the temperature $T_\infty = -5$ °C, and LWC = 2.0 g/m^3. Due to the warmer temperature and higher *LWC* for the test cases, while only a portion of the impinged water droplets was found to be frozen into ice immediately upon impacting onto the cable surfaces, the rest of the impacted water mass was found to be still in liquid. Driven by the freezing cold boundary layer airflow over the cable models, the unfrozen surface water was found to run back over the ice accreting surface, and then froze into ice subsequently at further downstream locations. As shown clearly in Fig. 5, the ice accretion on the cable models was found to form transparent, glassy ice structures with obvious traces of surface water runback, i.e., exhibiting typical glaze ice characteristics as described in Hansman and Kirby (1987). For the plain cable model C#1 (i.e., without helical fillets), similar as those described in Liu et al. (2019a), the unfrozen surface water film flow was found to break up into multiple rivulets while running back along the cable surface, and then froze into ice at further downstream locations to form rivulet-shaped runback ice structures. The irregular-shaped runback ice structures would protrude further into the incoming airflow to catch more runback water and airborne water droplets, which promoted a faster growth of the ice structures accreted over the cable surface (e.g., shown clearly in the snapshots acquired at $t = 100$s and $t = 200$s).

Due to the existence of the helical fillets, the ice accretion and runback process of the unfrozen surface water over the surfaces of the helical filleted cable models (i.e., models C#2, C#3 and C#4) were found to become very different, in comparison to those on the surface of the standard plain cable model (i.e., models C#1). Instead of moving streamwise to align with the incoming airflow direction over the surface of the plain cable model C#1, the unfrozen surface water was forced to flow along the edges of the helical fillets, and then freeze into ice eventually in front of the helical fillets. The blocked surface water would need to flow over the ridges of the helical fillets in order to be able to reach to further downstream regions, as shown in the dotted-line box in Fig. 5 (e.g., in the snapshot images acquired at t = 200s and t = 300s).

Corresponding to the different pitch lengths of the helical fillets wrapped over the cable surfaces, the unfrozen surface water was found to behave quite differently as running back over the cable surfaces. For the test models C#2 and C#3, since the orientation angles between the incoming airflow and the helical fillets are relatively larger, the runback surface water was found to be blocked by the helical fillets, causing the formation/accretion of glaze ice mainly in front of the helical fillets. Due to the formation of rather thick ice layer in front of the helical fillets for the test cases to effectively prevent the runback surface water from reaching further downstream regions, relatively large "clean" regions (i.e., the region without ice accretion) were observed behind the helical

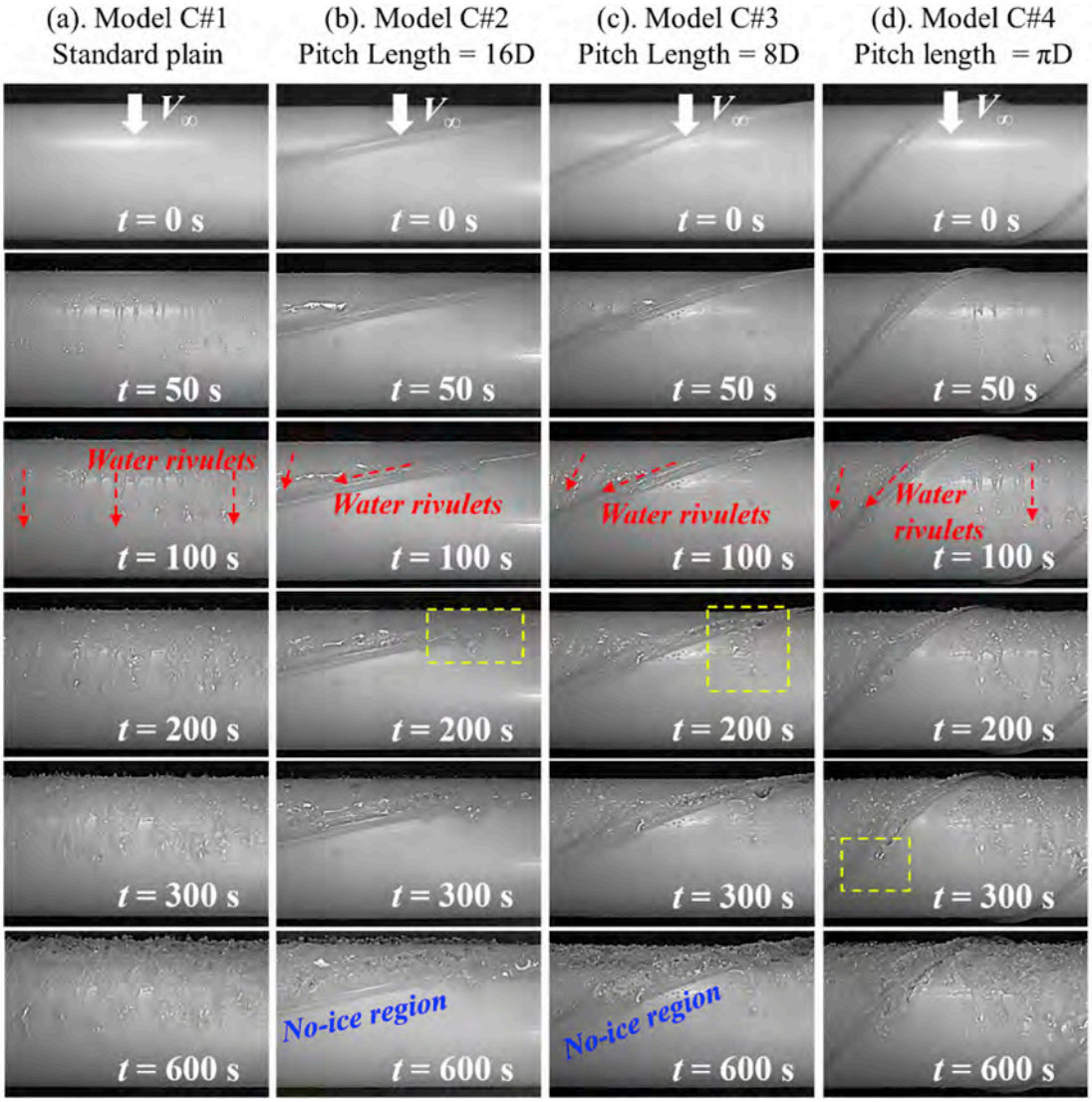

Fig. 5. Typical snapshots of the ice accretion on the cable models under the glaze icing condition.

fillets, as shown clearly in Fig. 5. However, for the model C#4 with the smallest helix pitch length, due to the relatively small orientation angle between the helical fillets and the incoming airflow, only a small portion of the runback water was found to be blocked in front of the helical fillets. Most of the surface water was found to be able to flow freely along the direction of the incoming airflow, resulting in the formation/accretion of the glaze ice structures over most of the rear surface of the cable model, including the regions behind the helical fillets.

3.2. Further analysis of the ice accretion processes over the surfaces of the cable models

Further efforts were made to quantify the ice thickness development over the leading edge of the four cable models during the ice accretion processes. It is well known that, the light intensity information scattered or reflected from the cable surfaces, water, and ice was included in the acquired snapshots of the ice accretion images. By deriving the changes in the intensity maps in the time sequences of acquired ice accretion images, Waldman and Hu (2016) developed an image processing algorithm to quantitatively extract the feature evolution of the dynamic ice accretion process over an airfoil model. Liu et al. (2018) adopted the similar algorithm to quantify the ice accretion process over rotating propeller blades. Following the work of Waldman and Hu (2016) and Liu et al. (2018), development of the ice layer accreted along the leading edges of cable models was determined quantitatively based on the time sequences of acquired ice accretion images.

As described in Waldman and Hu (2016) and Liu et al. (2018), the intensity difference maps for the images of the iced cable can be described by the following equation:

$$I^i_{\mathrm{ref}} = I^i - I^0 \tag{1}$$

where I^i is the ith image acquired as ice accreted over the cable surface and I^0 is the initial reference image of the cable (i.e., the cable surface without water or ice).

The intensity difference caused by the accumulation of water or ice accretion can be obtained by applying the image processing procedure mentioned above. Compared to the initial reference, the first location in front of the cable with a meaningful change in the pixel count can be identified. Through this method, the advancing front of the ice layer accreting along the leading edges of cables can be extracted, i.e., for every span position y,

$$x^i = \mathrm{first}\left(I^i_{\mathrm{ref}}(x)^2 > \varepsilon\right) \tag{2}$$

where ε is determined as the six standard deviations of the typical image noise in the present study. The image noise was characterized by calculating the root-mean-square (RMS) values of the pixel fluctuations between two successive images before ice accretion.

Then, the cable leading-edge ice thickness (i.e., H^i) can be obtained by the following equation:

$$H^i = K\left(x^i - x^i_0\right) \tag{3}$$

where x^i_0 is the initial pixel location of the cable leading edge and K is the calibration constant in mm/pixel (i.e., 0.115 mm/pixel in the present study).

The leading-edge ice thickness of the cable models can be quantitatively extracted by using the image processing method mentioned above. Figs. 6 and 7 show the time evolutions of the mean leading-edge ice thickness accreted on the cable models under the rime icing condition and glaze icing condition, respectively.

The measurement results given in Fig. 6 reveal clearly that, the thickness of the ice layers accreted along the leading edges of all the four cable models were found to increase almost linearly with the increasing ice accretion time under the rime icing condition. After the same period

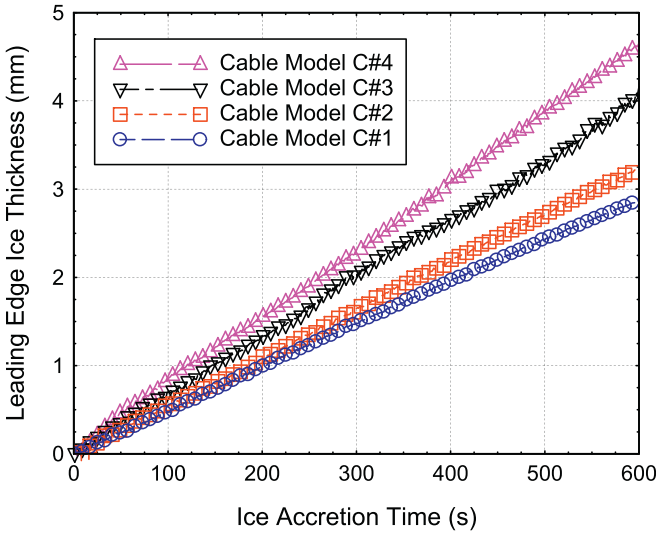

Fig. 6. Time evolution of the ice thickness accreted on the leading edges of the cable models under the rime icing condition.

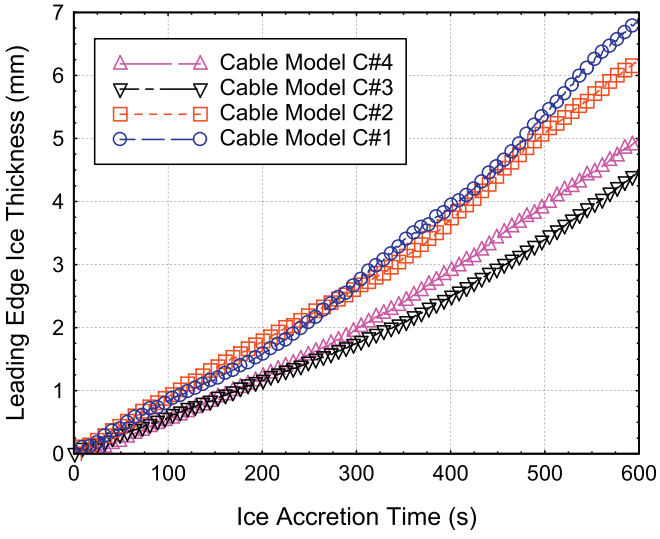

Fig. 7. Time evolution of the ice thickness accreted on the leading edges of the cable models under the glaze icing condition.

of the icing experiments, the ice layers accreted along the leading edges of the helical filleted cable models (i.e., models C#2, C#3 and C#4) were found to be thicker than that on the standard plain cable model (i.e., model C#1). While the growth rate of ice layer accreted along the leading-edge of the plain cable model C#1 was found to be about 0.0048 mm/s, the corresponding values were found to approximately 0.0054 mm/s, 0.0069 mm/s and 0.0078 mm/s for the helical filleted cable models C#2, C#3 and C#4, respectively. It can be seen clearly, that the cable model C#4, which has the smallest pitch of helical fillets, was found to have the fastest leading-edge ice growth rate. The cable model C#2, the model the longest pitch of helical fillets, was found to have the slowest ice growth rate among the three compared helical filleted cable models. In indicates that the growth rate of the ice layer accreted along the leading edge of the helical filleted cable models would increase as the pitch of helical fillets decreases.

As shown clearly in Fig. 7, the thickness variation characteristics of the ice layers accreted along the leading-edges of the cable models under the glaze icing condition were found to become significantly different from those under the rime icing condition. The leading-edge ice thickness

was still found to increase almost linearly only at the initial stage (i.e., within the first 200 s) of the glaze ice accretion experiments. However, at the later stage of the stage of the ice accretion experiments (i.e., after 200 s), the ice layers accreted along the cable leading edges were found to grow much faster with the increasing ice accretion time, i.e., growing in a nonlinear fashion, for all the test cases. Such growth characteristics of the ice layers accreted on the cable models are believed to be closely related to the formation/accretion of large, irregular-shaped ice structures, i.e., ice bumps, over the cable surfaces at the later stage of the glaze icing experiment. As shown clearly from the ice accretion images given in Fig. 5, the formation/accretion of large ice bumps near the cable leading edges under the glaze icing condition would enable the accreted ice structures protruding further into the incoming airflow, thereby, capturing more airborne water droplets to accelerate the ice accretion process. Therefore, the growth of the ice layers accreted over the surfaces of the cable models was found to increase rapidly in a nonlinear fashion at the later stage of the glaze icing experiments. It can also be seen that, due to the much higher *LWC* level used for the glaze icing experiments, the ice layers accreted on the cable models were found to become much thicker after the same duration (e.g., 600 s) of the ice accretion experiment, in comparison to those under the rime icing condition.

It was also found that, less amount of the glaze ice was accreted along the leading edges of the helical filleted cable models than that on the standard plain cable model. This can be explained by the fact that, the existence of the helical fillets would block the running back of the unfrozen surface water over the cable surfaces, and the accumulation of the unfrozen surface water would slow down the freezing process of the impinged water mass on the front surface of the cable models. The delay of the ice formation/accretion along the cable leading-edge region was found to be the most obvious for the helical filleted cable model C#3 (i.e., the model with the pitch length being 8*D*), having the slowest ice growth rate among the four compared test models. In summary, the experimental results suggest that the existence of the helical fillets would affect the glaze ice accretion process greatly, while the helical fillets wrapped around the cable surface at a certain pitch (e.g., pitch = 8D for the present study) would have the best effectiveness to delay the glaze ice accretion along the leading edge of the helical filleted cable.

3.3. Ice profile and volume extracted by three-dimensional scanning

A Digital Image Projection (DIP)-based 3D scanning system was also used in the present study to quantify the 3D shapes of the ice structures accreted over cable models after finishing the ice accretion experiments (i.e., at t = 600s). As described in Gao et al. (2019c), the DIP-based 3D scanning system is capable of measuring the complex 3D shapes of the ice structures accreted over the surfaces of the test models with a reasonable good measurement accuracy (i.e., about 0.2 mm). Veerakumar et al. (2020) used the same DIP-based 3D scanning system as one used in the present study to measure 3D roughness structures printed on a test plate. They found that the averaged difference between the measurement results and the nominal values was approximately 0.15 mm. In the present study, before conducting the cable icing experiments, the profiles of the "clean" cable models (i.e., without ice accretion) were scanned as the comparison baselines. By taking the helical filleted cable model C#4 as an example, Fig. 8 and Fig. 9 show the 3D scanning results at the end of the icing experiments under the rime icing condition and glaze icing condition, respectively. Based on the 3D scanning results, the cross-sectional profiles of the iced cable model at any selected cross-section locations can be extracted quantitatively. As shown schematically in Fig. 2, the representative cross sections of $\theta = 0°$, 45°, 90° and 135° were selected in the present study to extract the cross-sectional profiles of the iced cable.

As shown clearly in Fig. 8, the rime ice structures accreted over the surface of the cable model was found to be rather smooth, conforming the original profiles of the circular cable model in general. In comparison to the original circular shape of the cable model, the outer profile of the iced cable model was found to become more streamlined shape, leading to smaller aerodynamic drag force acting on the cable model, which will be

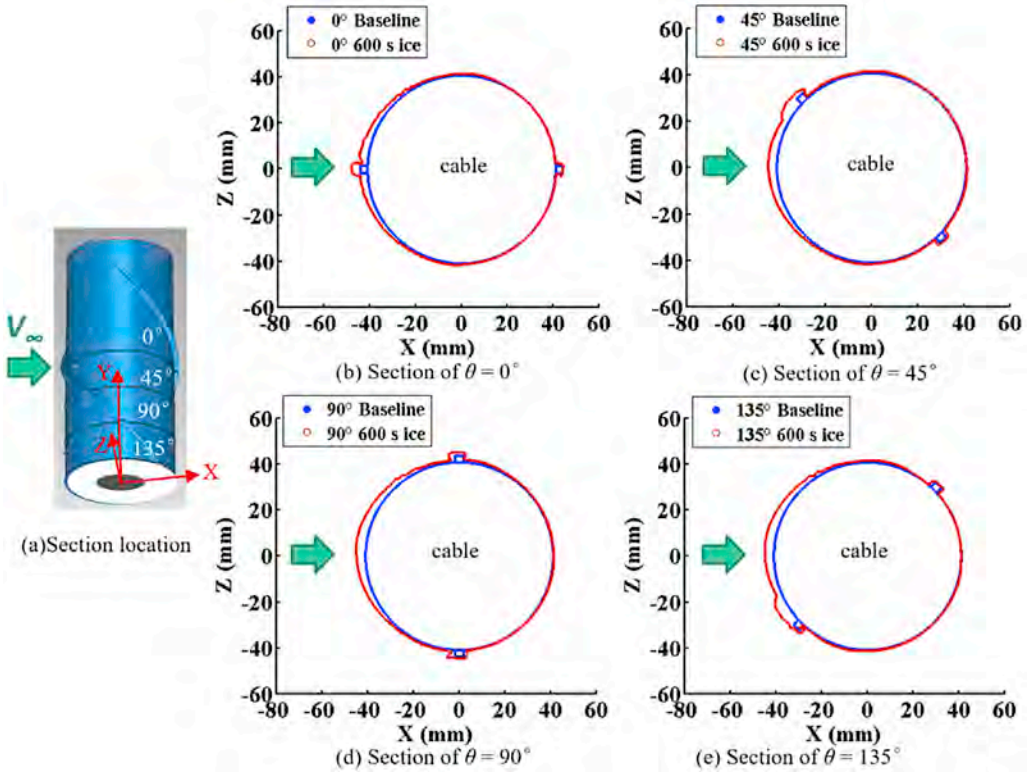

Fig. 8. 3D scanning results of the rime ice structures accreted on the cable model C#4 after 600 s of ice accretion experiment (a) the location of four sections; (b)~(e) the ice profiles at cross sections of $\theta = 0°$, $\theta = 45°$, $\theta = 90°$ and $\theta = 135°$ respectively.

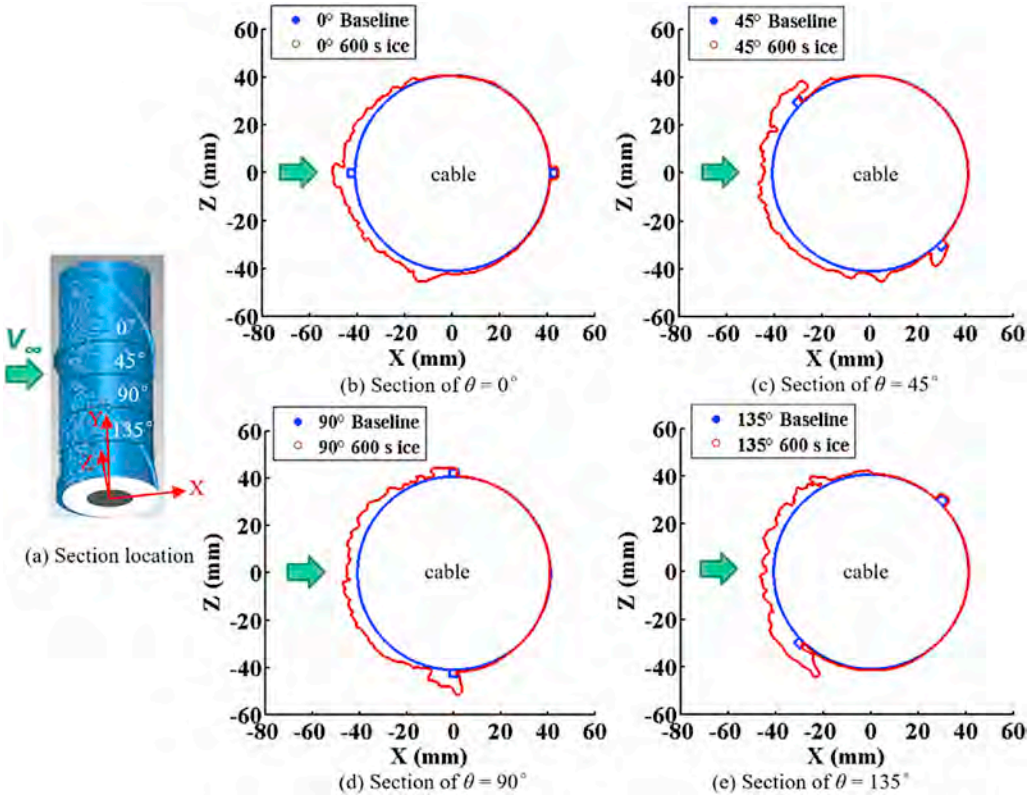

Fig. 9. 3D scanning results of the glaze ice structures accreted on the cable model C#4 after 600 s of ice accretion experiment (a) the location of four sections; (b)~(e) the ice profiles at cross sections of $\theta = 0°$, $\theta = 45°$, $\theta = 90°$ and $\theta = 135°$ respectively.

discussed in next section. It can also be seen that, more ice structures were found to accrete in front of the helical fillets, which agrees very well with the features revealed from the acquired snapshots of the ice accretion images given in Fig. 4. As clearly shown in Fig. 8(b) and (d), when the helical fillets were in the symmetrical position relative to the incoming airflow, the rime ice structures accreted over the cable surface were also found to be almost symmetrical in relation to the incoming airflow direction, as expected. In addition, the helical fillets shown in Fig. 8(c) were symmetrical to the helical fillets shown in Fig. 8(e), the rime ice structures accreted over the cable surface shown in Fig. 8(c) were found to be symmetrical to those shown in Fig. 8(e). The quantitative measurement results of the 3D shapes of the accreted ice structures reveal that, since the super-cooled water droplets carried by the incoming airflow would be frozen into ice instantly upon impinging onto the cable surface, the gravity force has almost no effects on the rime ice accretion process over the cable surface.

As shown clearly in Fig. 9, under the glaze icing condition, the outer profile of the iced cable model C#4 was found to remain as a cylindrical-shaped bluff body. The glaze ice structures accreted over the cable surface were found to become much rougher than those accreted under the rime icing condition. As mentioned above, under the glaze icing condition, while only a portion of the impinged water droplets would be frozen into solid ice instantly, and rest of the impinged water mass would stay in liquid phase. The unfrozen surface water would run back over the cable surfaces, as driven by the incoming airflow. Since the unfrozen surface water was forced to run back along the edges of the helical fillets wrapped around the cable surface, obviously thicker glaze ice layers were found to accrete in front of the helical fillets, as revealed clearly in Fig. 9. It was also revealed clearly that a portion of the unfrozen surface water would flow over the edges of the helical fillets and froze into ice subsequently. Since the existence of the helical fillets changed the moving path of the runback surface water over the cable surface, the thickness of the ice layer accreted over the cable model was found to vary significantly along the spanwise direction. The general shapes of glaze ice structures accreted over the cable surface were found to vary greatly, depending on the different locations of the helical fillets in the cross-sections. It can also be seen clearly that, under the effects of gravity forces, more glaze ice structures were found to accrete over the bottom side of the cable surface, in comparison to those over the top side of the cable surface.

Based on the quantitative measurement results of the 3D shapes of the ice structures, the total volumes of the ice layers accreted over the surfaces of the cable models can also be obtained by subtracting the volume of the "clean" cable (i.e., without ice) from the measured total volumes of the iced cables. Fig. 10 shows the comparison of the total amount of ice layers (i.e., volume) accreted on the four studied cable models under both

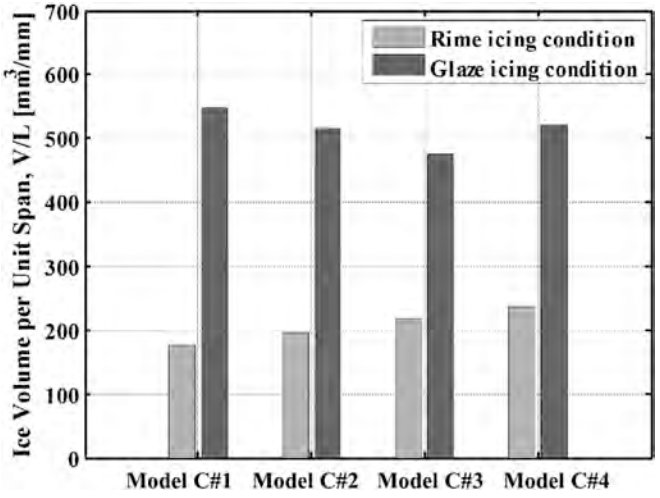

Fig. 10. The comparison of the total amount of the ice layers accreted over the surfaces of the cable models after 600 s of the ice accretion experiments.

rime and glaze ice conditions. It can be seen clearly that, For the same cable model and with the same duration of the ice accretion experiment, more ice structures were found to accumulate under the glaze icing condition than those under the rime icing condition, due to the higher liquid water content (LWC) level used for the glaze icing experiments. For the test cases of rime ice accretion, the total volumes of the ice structures accreted on the helical filleted cable models (i.e., models C#2, C#3 and C#4) were found to be greater than that on the standard plain cable model (i.e., model C#1). As the pitch length of the helical fillets decreased, the total volume of the accreted ice on the helical filleted cable model was found to increase monotonically. The helical filleted cable with the pitch length being πD (i.e., model C#4) was found to have the greatest ice accretion (i.e., largest total ice volume) among the four compared cable models. After 600 s of rime ice accretion experiment, the total volume of rime ice structures accreted on the helical filleted cable model C#4 was found to be about 23% more than that accreted on the standard plain cable (i.e., model C#1). However, under the glaze icing condition, the measured total volumes of the accumulated ice show very different characteristics. More glaze ice structures (i.e., greater total volume of the accreted ice layer) were found to accrete on the standard plain cable model than those on the helical filleted cable models. While the cable model with helical fillets of *8D* in pitch length (i.e., Model C#3) was found to have the least amount of the glaze ice accretion (i.e., smallest ice volume) among the four compared cable models, which is about 13% less than that on the standard plain cable model. The characteristics revealed from the measured total volumes of the ice structures accreted over the cable surfaces were found to be consistent very well with those revealed from the independently measured leading-edge ice thickness results described above.

3.4. Variations of the aerodynamic forces acting on the cable models during the icing process

As described above, the variations of the unsteady aerodynamic forces acting on the cable models during the ice accretion process were also measured in the present study by using two sets of high-sensitivity force/moment transducers mounted at the two ends of the cable models. The aerodynamic forces acting on the "clean" cable models (i.e., without any ice accretion) were measured at first before turning on the water spray system of ISU-IRT to start the ice accretion experiments, which were used as the reference cases to evaluate the effects of the ice accretion on the aerodynamic characteristics of the cable models. Since the measured lift forces acting on the cable models (i.e., vertical component of the aerodynamic forces) were found to be always very small (i.e., almost equal to zero), the variations of the drag forces (i.e., horizontal component of the aerodynamic forces) acting on the cable models during the ice accretion processes were the main focus of the present study. The drag coefficient of a cable model, C_d, is defined by using following equation:

$$C_d = \frac{F_d}{\frac{1}{2}\rho V_\infty^2 DL} \tag{4}$$

where F_d is the measured drag force acting on the cable model; D is the base diameter of the cable models; L is the spanwise length of the cable model; ρ is the density of airflow; and V_∞ represents the freestream velocity of the incoming airflow. To better illustrate the effects of the ice accretion on the drag coefficient of the cable models more clearly, the ratio *of* C_d/C_{d0} is calculated in the present study, where C_{d0} is the drag coefficient of the cable model before starting the ice accretion experiment. The measured drag coefficients of the "clean", helical-filleted cable models (i.e., C_{d0}) of the present study were found to agree very well with those reported by Kleissl and Georgakis (2012) for the bridge cables with helical fillets.

Fig. 11 shows the time evolution of the measured drag coefficients of the ice accreting cable models under the rime icing conduction. It can be seen clearly that, the drag forces acting on all the four cable models were found to decrease gradually as the ice accretion time increases. The drag decrease feature for the iced cable models under the rime icing condition is believed to be closely related to the observation of more "streamlined outer profiles" for the iced cable models, as revealed from the 3D ice shape measurement results given in Fig. 8. It can also be seen that, the drag coefficients of the helical filleted cable models (i.e., Models C#2, C#3 and C#4) were found to decrease at slower rates than that of the standard plain cable model C#1 under the same rime icing condition. For the three helical filleted cable models, the decrease rate of the aerodynamic drag force acting on the cable model was found to become slower as the pitch length of the helical fillets decreases. The drag force acting on the helical filleted cable model with the pitch length of $P = \pi D$ (i.e., the model C#4 with the smallest helical fillet pitch length) were found to have the least variations due to the rime ice accretion, i.e., decreasing only by about 5% after 600 s of rime ice accretion experiment. The drag forces acting on the standard plain cable model (i.e., the model C#1) was found to have the greatest drag reduction induced by the rime ice accretion. After 600 s of the ice accretion experiment, the aerodynamic drag acting on the plain cable model was found to become only about 75% of its original value (i.e., the drag acting on the "clean" cable model) due to the rime ice accretion.

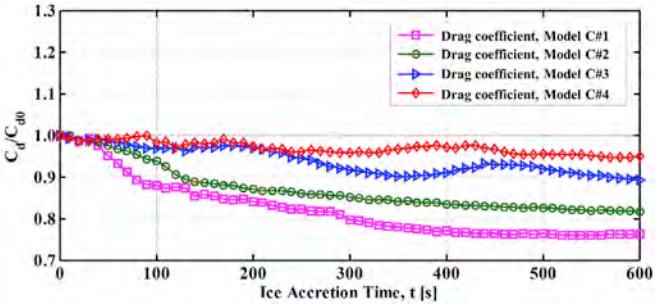

Fig. 11. Time evolution of the measured aerodynamic drag forces acting on the cable models during the rime ice accretion process.

Fig. 12 gives the measured aerodynamic drag acting on the iced cable models as a function of the ice accretion time under the glaze icing condition. The variation characteristics of the drag forces acting on the cable models due to the glaze ice accretion were found to become significantly different from those due to the rime ice accretion. The variations of the drag forces acting due to the glaze ice accretion can be divided into two stages for all the test models, i.e., 1) a drag decreasing stage at the beginning of the glaze icing process; and 2) a drag increasing stage at the later of glaze ice accretion process. At the first stage of the glaze icing process, the drag forces were found to decrease very rapidly for all the cable models. Among the four studied cable models, the drag acting on the standard plain cable model (i.e., model C#1) was found to have the greatest reduction due to the glaze ice accretion, i.e., reducing by 22% within the first 20 s. The drag forces acting on the helical filleted

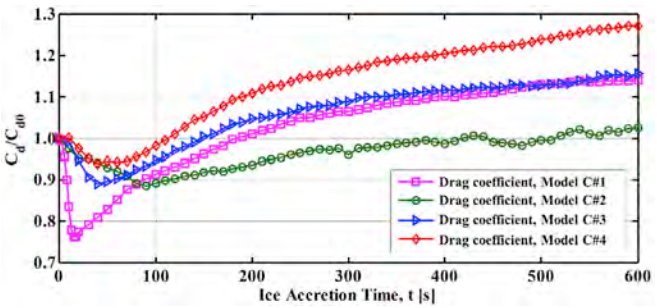

Fig. 12. Time evolution of the measured aerodynamic drag forces acting on the cable models during the glaze ice accretion process.

cable models were found to decrease at more moderate rates than that of the standard plain cable model. The time duration of the first stage (i.e., the time to reach the lowest drag coefficients) for the helical-filleted cable models were also found to be much longer than that of the standard plain cable model. The pitch length of the helical fillets was found to affect the variation characteristics of the drag forces acting on the helical-filleted cable models substantially. A helical-filleted cable model with a smaller helical pitch length was found to have a smaller drag reduction due to glaze ice accretion. More specifically, the helical filleted cable model C#4, which has the smallest helical pitch length, was found to have the least drag reduction, i.e., only decreased by 6% at the end of the first stage.

As shown in Fig. 12, the drag forces acting on all the cable models were found to increase gradually with the increasing ice accretion time at the later stage of the glaze icing experiment (i.e., the second stage). As described in Veerakumar et al. (2020), the continuous increase of the drag forces at the later stage of the glaze icing experiment is due to the thicker glaze ice layers accreted on the cable surfaces, thereby, enlarging the projected area of the iced cable models perpendicular to the incoming airflow direction. Furthermore, the formation of the irregular-shaped runback ice structures, i.e., ice bumps, over the cable surfaces would induce large-scale flow separations, which could also contribute to the continuous increase of the drag forces acting on the iced cable models at the later stage of the glaze icing experiment. It can also be seen that, the pitch length of the helical fillets would affect the variations of the drag forces acting on the helical-filleted cable models substantially. The cable model with a smaller pitch length of the helical fillets was found to have a greater drag increase due to the glaze ice accretion. Among the four compared cable models, the model C#4, which has the shortest pitch length of the helical fillets (i.e., $P = \pi D$) was found to have the greatest aerodynamic drag increase due to the glaze ice accretion. More specifically, the drag force acting on the cable model C#4 was found to increase to about 128% of its original value (i.e., the drag acting on the "clean" cable model) after 600 s of the glaze icing experiment. In comparison, the drag force acting on the standard plain cable model (i.e., cable model C#1) was found to increase to 114% of its original value after same 600 s of the glaze icing experiment.

3.5. PIV measurements to quantify the wake flow characteristics behind the cable models

In the present study, a high-resolution digital Particle Image Velocimetry (PIV) system was also used to quantify the changes of the wake flows behind the cable models during the dynamic ice accretion process.

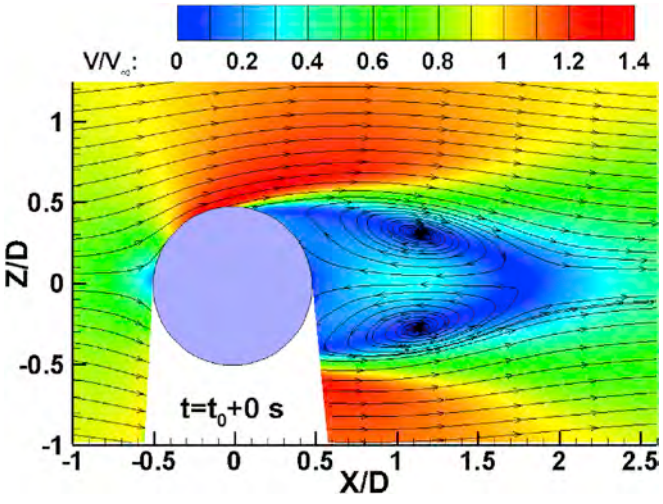

Fig. 13. Ensemble-averaged PIV measurement result to reveal the wake flow behind the "clean" plain cable model C#1.

Fig. 13 shows the time-averaged PIV measurement results in terms of the airflow velocity distribution along with the flow streamlines to reveal the wake characteristics behind the "clean" plain cable model C#1. While a large-scale symmetrical recirculating flow zone was observed as the dominant feature in the wake flow behind the "clean" plain cable model C#1, the flow separations took place in the symmetrical positions of the upper and lower cable section, as expected.

While Fig. 14 gives typical instantaneous PIV measurement results to reveal the unsteady vortex structures (i.e., in the term of normalized spanwise vorticity distributions) in the wake flow behind the "clean" helical filleted cable model C#3 with the helical pitch length of $P = 8D$, Fig. 15 shows the ensemble-averaged PIV measurement results to characterize the mean wake flow behind the helical filleted cable model C#3. PIV measurements were carried out at four typical cross sections (i.e., $\theta = 0°$, 45°, 90° and 135° as shown schematically in Fig. 2) along the longitudinal direction of the helical filleted cable model in order to better reveal the effects of the helical fillets wrapped round the cable surface on the wake flow behind the cable model. It can be seen clearly that, similar as that behind the standard plain cable model, a large-scale recirculating zone was also observed in the wake behind the helical filleted cable model. However, unlike the wake flow behind the standard plain cable model, the wake flow behind the helical filleted cable model C#3 was found to be completely asymmetric due to the existence of the helical fillets wrapped around the cable surface. Corresponding to the existence of the helical fillets located at different azimuthal positions in different cross-sections (i.e., $\theta = 0°$, 45°, 90° and 135°), the wake flow was found to be deflected at different angles. It can be seen clearly that, since the development of the boundary layer flow over the front surface of the cable model would be affected greatly by the existence of the helical fillets, the locations of the flow separation points and the shedding of the unsteady wake vortices from the cable model were found to change significantly in the different cross-sections behind the same helical filleted cable model. The asymmetric feature of the wake flow around the helical filleted cable model is expected to affect the uniformity of the ice accretion over the cable surface, which was revealed clearly from the acquired snapshots of the ice accretion images given in Figs. 6 and 7.

PIV measurements were also conducted to characterize the changes of the wake flows behind the cable models induced by the ice accretion over the cable surfaces for a better understanding of the variation characteristics of the aerodynamic forces acting on the cable models. For the PIV measurements to quantify the wake flow changes in the course of the dynamic ice accretion process, the switch of the water spray system of ISU-IRT was used to trigger the PIV system to conduct PIV measurements at pre-selected time instants (e.g., at $t = 0$, 50,100, 200, 300 and 600 s after starting the icing experiment). Fig. 16 shows typical PIV measurement results to reveal the changes of the wake flow behind the cable model C#3 induced by the ice accretion in the cross section of $\theta = 45°$ under the rime icing condition. As shown clearly by the PIV measurement results, while more rime ice structures would accrete over the cable surface as the ice accretion time increases, the recirculating zone in the wake behind the cable model C#3 was found to become smaller (e.g., Fig. 16(b) and (c)) in comparison to that behind the "clean" cable model in the first 100 s. After 100 s of ice accretion experiments (i.e., ice filling the steps between the leading edge of the helical fillets and the cable surface), the recirculating regions were found to be elongated and extended to further downstream, as revealed in Fig. 16(d), (e) and (f). The smaller and/or narrower recirculating zone behind the cable model would indicate less momentum deficits in the wake flow, thereby, smaller drag force acting on the cable model. The continuous drag reduction feature during the rime ice accreting process revealed from the PIV measurements was found to be consistent with the aerodynamic force measurement results obtained independently by using a pair of force/moment transducers mounted at the two end of the test model (i.e., the aerodynamic drag data given in Fig. 11).

Fig. 17 shows the typical PIV measurements results to reveal the dynamic changes of the wake flow behind the helical filleted cable model

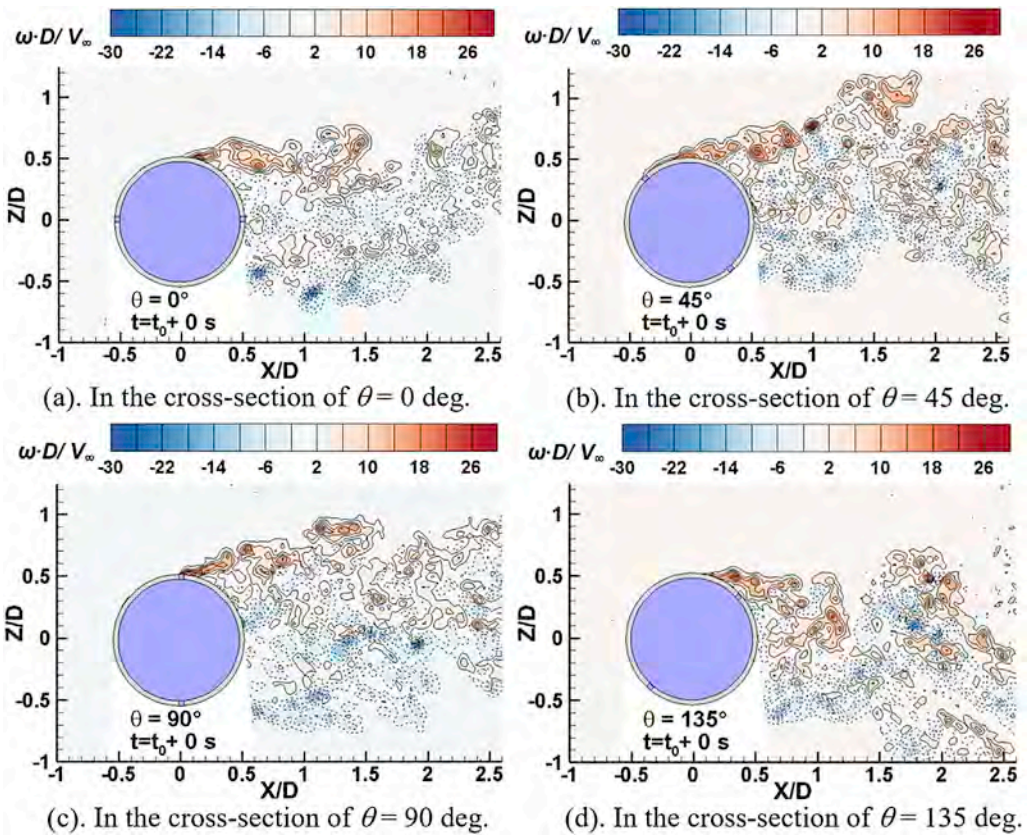

Fig. 14. Instantaneous PIV measurement results to reveal the unsteady vortex structures in the wake flow behind the "clean" helical filleted cable model C#3 with the helical pitch length of $P = 8D$.

C#3 in the course of the glaze ice accreting process. It was revealed clearly that, in comparison to that behind the "clean" cable model, the recirculating zone in the wake behind the cable model C#3 was found to become much smaller and narrower at the initial stage of the glaze icing process. The observation can be explained by the fact that, the ice layer accreted on the test model is very thin and smooth at the initial stage of the glaze icing process (i.e., $t < 60$s for the present study). The existence of the thin runback water film would affect the development of the boundary layer airflow over the cable surface greatly. In comparison to the "dry" surface case (i.e., without runback water on the cable surface), the thin runback water film over the cable surface could act as a "lubricant" layer to make the airflow moving more smoothly around the "wet" cable surface. It would make the "wet" cable surface becoming a "slip" surface for the boundary layer airflow, thereby, delay the separation of the boundary layer airflow from the "wet" cable surface. As a result, in comparison to that behind "clean" cable model, the size of the recirculating zone in the wake behind the cable model was found to decrease greatly at the initial stage of the glaze ice accretion process, as shown clearly in Fig. 17(b). The smaller size of the recirculating zone would imply less monument deficits in the wake flow, thereby, smaller aerodynamic drag force acting on the cable model induced by the ice accretion at the initial stage of the glaze icing process. The PIV measurement results can be used to clearly explain the drag reduction feature at the initial stage of the glaze icing process revealed from the aerodynamics drag measurement data given in Fig. 12.

As the ice accretion time increases, with more super-cooled water droplets impinging onto the cable surface, the glaze ice layer accreted over the surface of the cable model would become much thicker. As revealed clearly from the snapshots of ice accretion images given in Fig. 5, the surface of the iced cable model would become much rougher with the formation of more irregular-shaped ice humps (i.e., runback ice structures) over the cable surface at the later stage of the glaze icing process. The formation of the irregular-shaped runback ice structures over the cable surface would induce large-scale flow separation, resulting in the bigger and wider recirculating zone in the wake behind the cable model, as revealed clearly from the PIV measurement results given in Fig. 17. The bigger and wider recirculating zone in the wake flow would suggest much greater momentum deficits in the wake flow, thereby, greater aerodynamic drag force acting on the cable model induced by the ice accretion at the later stage of the glaze icing process. The drag increasing feature revealed from the PIV measurements at the later stage of the glaze icing process was confirmed quantitatively by the aerodynamics drag measurement results given in Fig. 12.

4. Conclusions

In the present study, a comprehensive experimental investigation was conducted to characterize the dynamic ice accretion process over the surfaces of bridge stay cables with and without helical fillets and to examine the effects of the ice accretion on the aerodynamic characteristics of the stay cables under typical rime and glaze icing conditions. The experimental study was performed by leveraging the Icing Research Tunnel of Iowa State University (i.e., ISU-IRT) to simulate typical dry rime icing and wet glaze icing conditions that bridge stay cables are usually exposed to in cold weather. Four cable models, i.e., one standard plain cable model and three cable models wrapped with helical fillets over the cable surfaces at different pitch lengths, were used for a comparative study. In addition to using a high-speed imaging system to record the dynamic ice accretion process over the surfaces of the cable models, a digital image projection (DIP) based, three-dimensional (3D) scanning technique was also utilized to quantify the 3D shapes of the ice structures accreted on the cable models. While a high-resolution digital Particle Image Velocimetry (PIV) system was used to characterize the wake flows behind the cable models during the ice accreting process, the

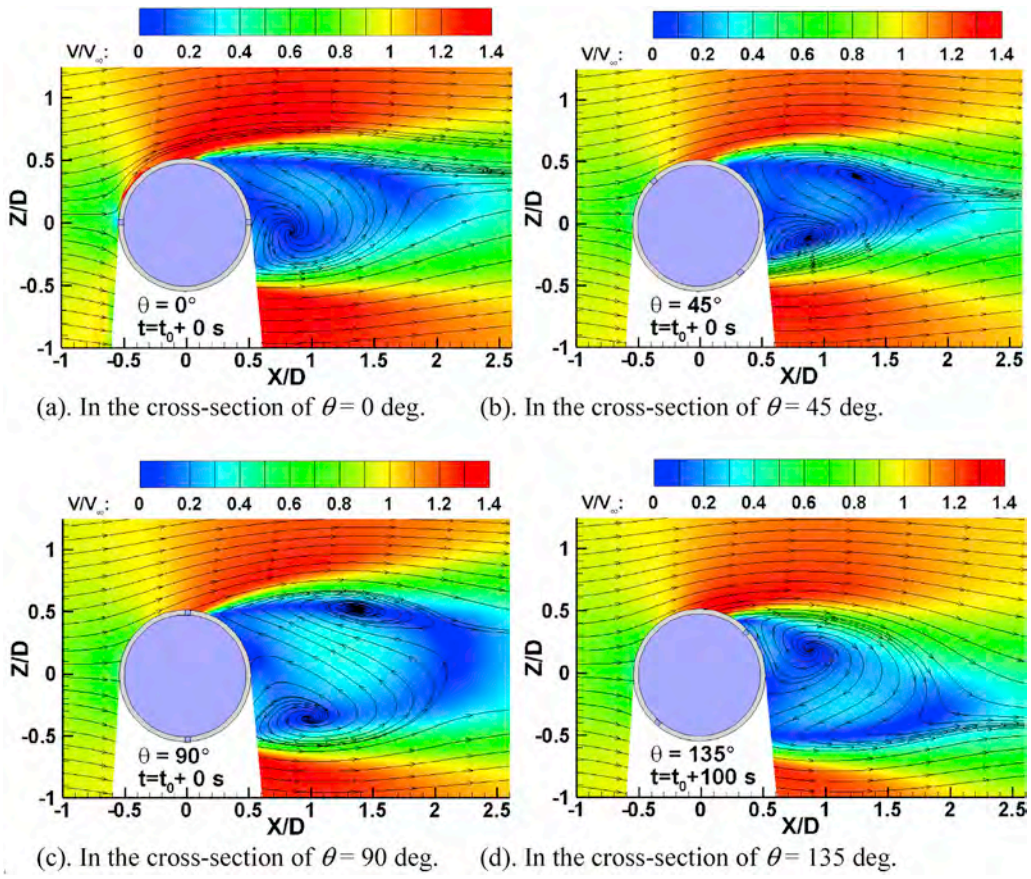

(a). In the cross-section of $\theta = 0$ deg. (b). In the cross-section of $\theta = 45$ deg.

(c). In the cross-section of $\theta = 90$ deg. (d). In the cross-section of $\theta = 135$ deg.

Fig. 15. The ensemble-averaged PIV measurement results to reveal the wake flow behind the "clean" helical filleted cable model C#3 with the helical pitch length of $P = 8D$.

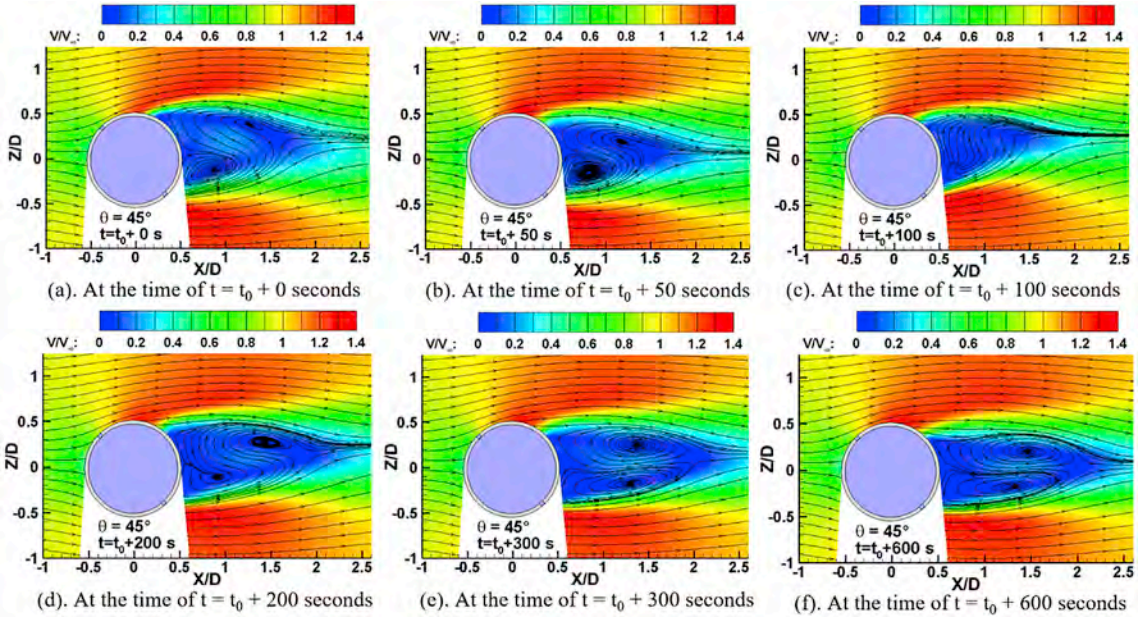

(a). At the time of $t = t_0 + 0$ seconds (b). At the time of $t = t_0 + 50$ seconds (c). At the time of $t = t_0 + 100$ seconds

(d). At the time of $t = t_0 + 200$ seconds (e). At the time of $t = t_0 + 300$ seconds (f). At the time of $t = t_0 + 600$ seconds

Fig. 16. PIV measurements of the wake flow behind the cable model C#3 in the cross section of $\theta = 45°$ during the rime ice accreting process.

time variations of the aerodynamic drag forces acting on the test models were also measured by using a pair of high-sensitive force/moment transducers mounted at two ends of the cable models.

Under the rime icing condition of $V_\infty = 20$ m/s, $T_\infty = -15$ °C, and $LWC = 1.0$ g/m^3, almost all the super-cooled water droplets were found to be frozen into solid ice instantly, upon impinging onto the cable surfaces. More ice structures were found to accrete over the surfaces of the helical filleted cable models, in comparison to those on the plain cable model. Both the thickness of the ice layer accreted along the cable leading edges and the total amounts of the rime ice structures accreted

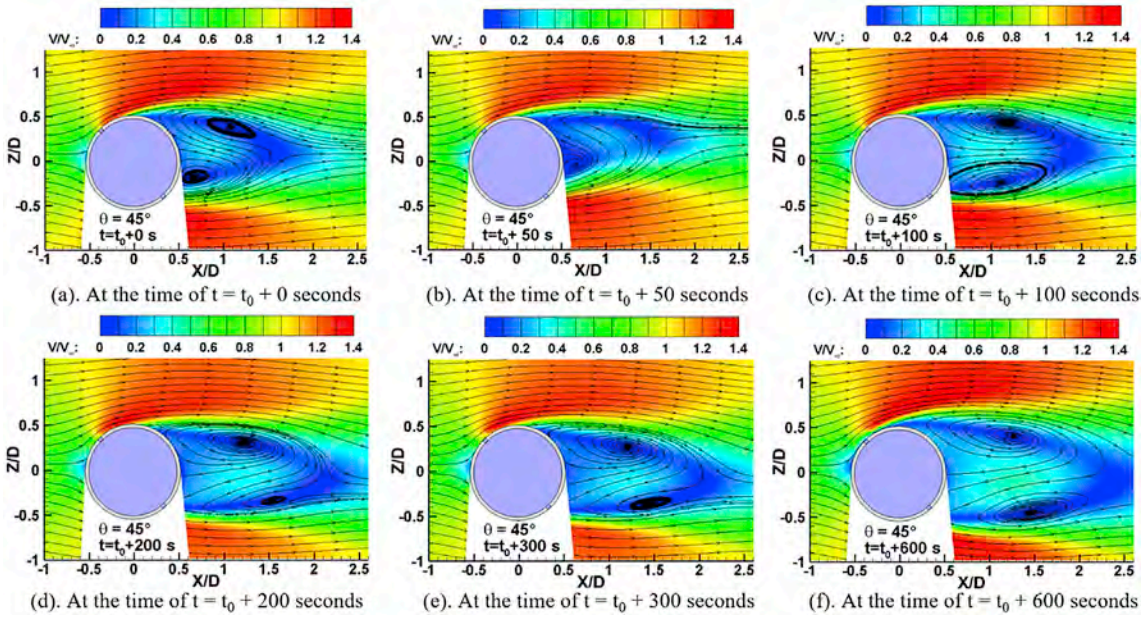

Fig. 17. PIV measurements of the wake flow behind the cable model C#3 in the cross section of $\theta = 45^{\circ}$ during the glaze ice accreting process.

over the surfaces of the helical filleted cable models were found to increase monotonically with the decreasing pitch length of the helical fillets. More specifically, after 600 s of rime ice accretion experiment, about 23% more ice structures (i.e., by volume) were found to accrete over the surface of the helical filleted cable model with the helical pitch length being πD (where D is the cable diameter), in comparison to those on the standard plain cable model.

Under the glaze icing condition of $V_{\infty} = 20$ m/s, $T_{\infty} = -5$ °C, and $LWC = 2.0$ g/m^3, upon impinging onto the cable surfaces, only a portion of the super-cooled water droplets would be frozen into solid ice instantly. The rest of the impacted water droplets was found to stay in liquid to form a thin water film over the front surfaces of the cable models, which can move freely over the cable surfaces. As driven by the frozen-cold airflow around the cable models, the unfrozen surface water was found to run back swiftly to reach further downstream regions, and freeze into ice subsequently to form irregular-shaped runback ice structures on the rear surface of the plain cable model. For the helical filleted cable models, since the existence of the helical fillets wrapped around the cable surfaces would block the runback unfrozen water flow, most of the surface water was forced to flow along the edges of the helical fillets. Therefore, significant amount of glaze ice structures were observed to accrete in front of the helical fillets. The accumulation of the unfrozen surface water in front of the helical fillets was found to delay the freezing process of the impinged super-cooled water droplets on the cable surfaces. As a result, less amount of the glaze ice was found to accrete over the cable surfaces wrapped with helical fillets, in comparison to that over the standard plain cable surface. The pitch length of helical fillets was also found to affect the glaze ice accretion process over the cable surface substantially. More specifically, after 600 s of ice accretion experiment, the total amount of the glaze ice structures accreted on the helical filleted cable model with the pitch length being 8D was found to be approximately 13% less (i.e., by volume) than those accreted on the standard plain cable model.

The aerodynamic force measurements results reveal clearly that, with the rime ice structures accreting over the cable surfaces, the aerodynamic drag forces acting on all the cable models were found to decrease continuously as the ice accretion time increases. While the drag decreasing rates for the helical filleted cable models were found to be substantially smaller than that of the standard plain cable model, the extent of the drag reduction due to the rime ice accretion on the helical filleted cable models was found to increase gradually as the pitch length of the helical fillets decreases. After 600 s of rime ice accretion experiment, while the aerodynamic drag force acting on the standard plain cable model was found to decrease by 24%, the corresponding drag force reduction due to the rime ice accretion on the helical filleted cable model with the helical pitch length being πD was found to be only about 5%.

Under the glaze icing condition, the aerodynamic drag forces acting on the cable models were found to decrease quickly at the initial stage of the icing process, and then increase gradually with the increase ice accretion time at the later stage of the glaze ice accreting process. More specifically, the aerodynamic drag force acting on the plain cable model was found to decrease by 22% at the initial stage of the glaze icing process (i.e., within the first 20 s), and then increase continuously up to 114% of its original value after 600 s of the glaze icing experiment. In comparison, the drag reduction at the initial stage of the glaze icing process was found to be only about 6% for the helical filleted cable model with the helical fillet pitch length being πD, and then increase up to 127% of its original value after the same 600 s of the glaze icing experiment.

The PIV measurement results reveal clearly that, the flow characteristics in the wakes behind the cable models would change significantly due to the ice accretion over the cable surfaces. The quantitative PIV measurement results are very helpful to elucidate the underlying physics for a better understanding of the different variation characteristics of the aerodynamic forces acting on the cable models under different icing conditions.

In summary, the findings of the present study reveal clearly that the existence of helical fillets over the surfaces of bridge cables would affect the dynamic ice accretion process and the resultant aerodynamic performance of the cables significantly. It should be noted that, this is our first progress report of a comprehensive experimental campaign on bridge cable icing physics and anti-/de-icing. While the focus of the present study is on characterizing the effects of helical fillets on the ice accretion over the surfaces of bridge cables, more extensive studies about other important factors, such as the contaminations on the cable surfaces (i.e., the cleanliness of the cable surfaces), the uniformity and the turbulence levels of the incoming airflow, the yawing and inclination angles of the cables in relation to the incoming airflow direction will be explored in our future work.

Authorship contribution statement

Yihua Peng: Icing tunnel experiments, Model design and manufacture, Data acquisition and processing, Formal analysis, Writing - original draft. **Ramsankar Veerakumar:** Icing tunnel experiments, Data acquisition and processing. **Yang Liu:** Methodology, Data processing & analysis, Project administration. **Xuhui He:** Methodology, Funding acquisition, Supervision. **Hui Hu:** Conceptualization, Methodology, Formal analysis, Writing – review & editing, Funding acquisition, Supervision.

Declaration of competing interest

The authors declare that they have no known competing financial interests or personal relationships that could have appeared to influence the work reported in this paper.

Acknowledgements

The first author, YH Peng would like to thank China Scholarship Council to support his visit to Iowa State University. This research work is partially support by National Science Foundation (NSF) of USA under award numbers of OISE-1826978 and CBET-1916380. The support from National Natural Science Foundations of China (No. U1534206, 51708559, 51925808) and National Key Research and Development Plan Project of China (subproject 2017YFB1201204) to YH Peng and XH He is also acknowledged.

References

Achenbach, E., Heinecke, E., 1981. On vortex shedding from smooth and rough cylinders in the range of Reynolds numbers 6000 to 5000000. J. Fluid Mech. 109, 239–251. https://doi.org/10.1017/s002211208100102x.

Barlow, J.B., Rae, J.W.H., Pope, A., 1999. Low Speed Wind Tunnel Testing, third ed. John Wiley & Sons.

Benidir, A., Flamand, O., Gaillet, L., Dimitriadis, G., 2015. Impact of roughness and circularity-defect on bridge cables stability. J. Wind Eng. Ind. Aerod. 137, 1–13. https://doi.org/10.1016/j.jweia.2014.11.010.

Benidir, A., Flamand, O., Dimitriadis, G., 2018. The impact of circularity defects on bridge stay cable dry galloping stability. J. Wind Eng. Ind. Aerod. 181, 14–26. https://doi.org/10.1016/j.jweia.2018.08.009.

Bragg, M.B., Broeren, A.P., Blumenthal, L.A., 2005. Iced-airfoil aerodynamics. Prog. Aero. Sci. 41, 323–362. https://doi.org/10.1016/j.paerosci.2005.07.001.

Buresti, G., 1981. The effect of surface roughness on the flow regime around circular cylinders. J. Wind Eng. Ind. Aerod. 8, 105–114. https://doi.org/10.1016/0167-6105(81)90011-8.

Cao, S., Jalali, H.H., Dragomirescu, E., 2018. Wind-induced response of inclined and yawed ice-accreted stay cable models. Shock Vib. 2018, 1–12. https://doi.org/10.1155/2018/6853047.

Caracoglia, L., Jones, N.P., 2007. Passive hybrid technique for the vibration mitigation of systems of interconnected stays. J. Sound Vib. 307, 849–864. https://doi.org/10.1016/j.jsv.2007.07.022.

Caracoglia, L., Zuo, D., 2009. Effectiveness of cable networks of various configurations in suppressing stay-cable vibration. Eng. Struct. 31, 2851–2864. https://doi.org/10.1016/j.engstruct.2009.07.012.

Chen, Z.Q., Wang, X.Y., Ko, J.M., Ni, Y.Q., Spencer, B.F., Yang, G., Hu, J.H., 2004. MR damping system for mitigating wind-rain induced vibration on Dongting Lake cable-stayed bridge. Wind Struct. 7, 293–304. https://doi.org/10.12989/was.2004.7.5.293.

Chen, W., Xin, D., Xu, F., Li, H., Ou, J., Hu, H., 2013. Suppression of vortex-induced vibration of a circular cylinder using suction-based flow control. J. Fluid Struct. 42, 25–39. https://doi.org/10.1016/j.jfluidstructs.2013.05.009.

Chen, W., Li, H., Hu, H., 2014. An experimental study on a suction flow control method to reduce the unsteadiness of the wind loads acting on a circular cylinder. Exp. Fluid 55 (4), 1707. https://doi.org/10.1007/s00348-014-1707-7, 20 pages.

Chen, W., Chen, G., Xu, F., Huang, Y., Gao, D., Li, H., 2020. Suppression of vortex-induced vibration of a circular cylinder by a passive-jet flow control. J. Wind Eng. Ind. Aerod. 199, 104119. https://doi.org/10.1016/j.jweia.2020.104119.

Christiansen, H., Jakobsen, J.B., Macdonald, J.H.G., Larose, G.L., Bosch, H.R., 2018a. Aerodynamics of a stay cable with helical fillets - Part I: stability and load characteristics. J. Wind Eng. Ind. Aerod. 177, 376–391. https://doi.org/10.1016/j.jweia.2018.01.045.

Christiansen, H., Jakobsen, J.B., Macdonald, J.H.G., Larose, G.L., Bosch, H.R., 2018b. Aerodynamics of a stay cable with helical fillets - Part II: fluctuating load and wake characteristics. J. Wind Eng. Ind. Aerod. 177, 392–404. https://doi.org/10.1016/j.jweia.2018.01.044.

Demartino, C., Ricciardelli, F., 2015. Aerodynamic stability of ice-accreted bridge cables. J. Fluid Struct. 52, 81–100. https://doi.org/10.1016/j.jfluidstructs.2014.10.003.

Demartino, C., Ricciardelli, F., 2017. Aerodynamics of nominally circular cylinders: a review of experimental results for Civil Engineering applications. Eng. Struct. 137, 76–114. https://doi.org/10.1016/j.engstruct.2017.01.023.

Demartino, C., Koss, H.H., Georgakis, C.T., Ricciardelli, F., 2015. Effects of ice accretion on the aerodynamics of bridge cables. J. Wind Eng. Ind. Aerod. 138, 98–119. https://doi.org/10.1016/j.jweia.2014.12.010.

Farell, C., 1981. Flow around fixed circular cylinders: fluctuating loads. J. Eng. Mech. Div. 107, 565–588.

Flamand, O., 1995. Rain-wind induced vibration of cables. J. Wind Eng. Ind. Aerod. 57, 353–362.

Gao, L., Liu, Y., Hu, H., 2019a. An experimental investigation of dynamic ice accretion process on a wind turbine airfoil model considering various icing conditions. Int. J. Heat Mass Tran. 133, 930–939. https://doi.org/10.1016/j.ijheatmasstransfer.2018.12.181.

Gao, L., Liu, Y., Zhou, W., Hu, H., 2019b. An experimental study on the aerodynamic performance degradation of a wind turbine blade model induced by ice accretion process. Renew. Energy 133, 663–675. https://doi.org/10.1016/j.renene.2018.10.032.

Gao, L., Veerakumar, R., Liu, Y., Hu, H., 2019c. Quantification of the 3D shapes of the ice structures accreted on a wind turbine airfoil model. J. Visual 22 (4), 661–667. https://doi.org/10.1007/s12650-019-00567-4.

Ge, Y., Chang, Y., Xu, L., Zhao, L., 2018. Experimental investigation on spatial attitudes, dynamic characteristics and environmental conditions of rain–wind-induced vibration of stay cables with high-precision raining simulator. J. Fluid Struct. 76, 60–83. https://doi.org/10.1016/j.jfluidstructs.2017.09.006.

Gjelstrup, H., Georgakis, C.T., Larsen, A., 2012. An evaluation of iced bridge hanger vibrations through wind tunnel testing and quasi-steady theory. Wind Struct. Int. J. 15, 385–407. https://doi.org/10.12989/was.2012.15.5.385.

Gorski, P., Pospisil, S., Kuznetsov, S., Tatara, M., Marusic, A., 2016. Strouhal number of bridge cables with ice accretion at low flow turbulence. Wind Struct. 22, 253–272. https://doi.org/10.12989/was.2016.22.2.253.

Gu, M., Du, X., 2005. Experimental investigation of rain-wind-induced vibration of cables in cable-stayed bridges and its mitigation. J. Wind Eng. Ind. Aerod. 93, 79–95. https://doi.org/10.1016/j.jweia.2004.09.003.

Güven, O., Farell, C., Patel, V.C., 1980. Surface-roughness effects on the mean flow past circular cylinders. J. Fluid Mech. 98, 673–701. https://doi.org/10.1017/S0022112080000341.

Hansman, R.J., Kirby, M.S., 1987. Comparison of wet and dry growth in artificial and flight icing conditions. J. Thermophys. Heat Tran. 1, 215–221. https://doi.org/10.2514/3.30.

Hartog, J.P.D., 1932. Transmission Line Vibration Due to Sleet, vol. 51. Transactions of the American Institute of Electrical Engineers, pp. 1074–1076. https://doi.org/10.1109/T-AIEE.1932.5056223.

Hikami, Y., Shiraishi, N., 1988. Rain-wind induced vibrations of cables stayed bridges. J. Wind Eng. Ind. Aerod. 29, 409–418. https://doi.org/10.1016/0167-6105(88)90179-1.

Hua, J., Zuo, D., 2019. Evaluation of aerodynamic damping in full-scale rain-wind-induced stay cable vibration. J. Wind Eng. Ind. Aerod. 191, 215–226. https://doi.org/10.1016/j.jweia.2019.06.008.

Ibrahim, G.M., Pope, K., Muzychka, Y.S., 2018. Effects of blade design on ice accretion for horizontal axis wind turbines. J. Wind Eng. Ind. Aerod. 173, 39–52. https://doi.org/10.1016/j.jweia.2017.11.024.

Jafari, M., Hou, F., Abdelkefi, A., 2020. Wind-induced vibration of structural cables. Nonlinear Dynam. 100, 351–421. https://doi.org/10.1007/s11071-020-05541-6.

Jing, H., Xia, Y., Li, H., Xu, Y., Li, Y., 2015. Study on the role of rivulet in rain–wind-induced cable vibration through wind tunnel testing. J. Fluid Struct. 59, 316–327. https://doi.org/10.1016/j.jfluidstructs.2015.09.008.

Jing, H., Xia, Y., Li, H., Xu, Y., Li, Y., 2017. Excitation mechanism of rain–wind induced cable vibration in a wind tunnel. J. Fluid Struct. 68, 32–47. https://doi.org/10.1016/j.jfluidstructs.2016.10.006.

Katsuchi, H., Yamada, H., Sakaki, I., Okado, E., 2017. Wind-tunnel investigation of the aerodynamic performance of surface-modification cables. Engineering 3, 817–822. https://doi.org/10.1016/j.eng.2017.09.001.

Kleissl, K., 2013. Cable Aerodynamic Control - Wind Tunnel Studies. Technical University of Denmark.

Kleissl, K., Georgakis, C.T., 2011. Aerodynamic control of bridge cables through shape modification: a preliminary study. J. Fluid Struct. 27, 1006–1020. https://doi.org/10.1016/j.jfluidstructs.2011.04.012.

Kleissl, K., Georgakis, C.T., 2012. Comparison of the aerodynamics of bridge cables with helical fillets and a pattern-indented surface. J. Wind Eng. Ind. Aerod. 104–106, 166–175. https://doi.org/10.1016/j.jweia.2012.02.031.

Koss, H., Lund, M.S.M., 2013. Experimental Investigation of Aerodynamic Instability of Iced Bridge Cable Sections. 6th European and African Wind Engineering.

Koss, H.H., Gjelstrup, H., Georgakis, C.T., 2012. Experimental study of ice accretion on circular cylinders at moderate low temperatures. J. Wind Eng. Ind. Aerod. 104–106, 540–546. https://doi.org/10.1016/j.jweia.2012.03.024.

Koss, H.H., Henningsen, J.F., Olsen, I., 2013. Influence of icing on bridge cable aerodynamics. Proceedings of the 15th International Workshop on Atmospheric Icing of Structures (IWAIS XV) 6–12, 16–18.

Li, X.M., Nie, X.C., Zhu, Y.K., Yi, Y., Yan, Z.T., 2017. Wind tunnel tests on aerodynamic characteristics of ice-coated 4-bundled conductors. Math. Probl Eng. 2017, 1–11. https://doi.org/10.1155/2017/1628173.

Li, L.K., Liu, Y., Tian, L.C., Hu, H.Y., Liu, X.J., Hogate, I., Kohli, A., Hu, H., 2020. An experimental study on a hot-air-based anti-/de-icing system for aero-engine inlet

guide vanes. Appl. Therm. Eng. 167, 114778. https://doi.org/10.1016/j.applthermaleng.2019.114778 (12 pages).
Liu, Y., Li, L., Ning, Z., Tian, W., Hu, H., 2018. Experimental investigation on the dynamic icing process over a rotating propeller model. J. Propul. Power 34, 933–946. https://doi.org/10.2514/1.B36748.
Liu, Y., Li, L., Chen, W., Tian, W., Hu, H., 2019a. An experimental study on the aerodynamic performance degradation of a UAS propeller model induced by ice accretion process. Exp. Therm. Fluid Sci. 102, 101–112. https://doi.org/10.1016/j.expthermflusci.2018.11.008.
Liu, Y., Chen, W., Peng, Y., Hu, H., 2019b. An experimental study on the dynamic ice accretion processes on bridge cables with different surface modifications. J. Wind Eng. Ind. Aerod. 190, 218–229. https://doi.org/10.1016/j.jweia.2019.05.007.
Ma, W., Liu, Q., Macdonald, J.H.G., Yan, X., Zheng, Y., 2019. The effect of surface roughness on aerodynamic forces and vibrations for a circular cylinder in the critical Reynolds number range. J. Wind Eng. Ind. Aerod. 187, 61–72. https://doi.org/10.1016/j.jweia.2019.01.011.
Makkonen, L., Poots, G., 2000. Models for the growth of rime, glaze, icicles and wet snow on structures. Philos. Trans. R. Soc. London, Ser. A: Mathematical, Physical and Engineering Sciences 358, 2913–2939. https://doi.org/10.1098/rsta.2000.0690.
Makkonen, L., Zhang, J., Karlsson, T., Tiihonen, M., 2018. Modelling the growth of large rime ice accretions. Cold Reg. Sci. Technol. 151, 133–137. https://doi.org/10.1016/j.coldregions.2018.03.014.
Matsumoto, M., Shiraishi, N., Shirato, H., 1992. Rain-wind induced vibration of cables of cable-stayed bridges. J. Wind Eng. Ind. Aerod. 43, 2011–2022. https://doi.org/10.1016/0167-6105(92)90628-N.
Matsumoto, M., Daito, Y., Kanamura, T., Shigemura, Y., Sakuma, S., Ishizaki, H., 1998. Wind-induced vibration of cables of cable-stayed bridges. J. Wind Eng. Ind. Aerod. 74–76, 1015–1027. https://doi.org/10.1016/S0167-6105(98)00093-2.
Matteoni, G., Georgakis, C.T., 2012. Effects of bridge cable surface roughness and cross-sectional distortion on aerodynamic force coefficients. J. Wind Eng. Ind. Aerod. 104–106, 176–187. https://doi.org/10.1016/j.jweia.2012.02.029.
Matteoni, G., Georgakis, C.T., 2015. Effects of surface roughness and cross-sectional distortion on the wind-induced response of bridge cables in dry conditions. J. Wind Eng. Ind. Aerod. 136, 89–100. https://doi.org/10.1016/j.jweia.2014.11.003.
McComber, P., Paradis, A., 1998. A cable galloping model for thin ice accretions. Atmos. Res. 46, 13–25. https://doi.org/10.1016/S0169-8095(97)00047-1.
Miyata, Y., Yamada, H., Hojo, T., 1994. Experimental study on aerodynamic characteristics of cables with patterned surface. J. Struct. Eng. 40, 1065–1076.
Naterer, G.F., 2011. Multiphase transport processes of droplet impact and ice accretion on surfaces. Cold Reg. Sci. Technol. 65, 5–12. https://doi.org/10.1016/j.coldregions.2009.09.005.
Poots, G., 1996. Ice and Snow Accretion on Structures. John Wiley and Sons Inc.
Ribeiro, J.D., 1991a. Effects of surface roughness on the two-dimensional flow past circular cylinders I: mean forces and pressures. J. Wind Eng. Ind. Aerod. 37, 299–309. https://doi.org/10.1016/0167-6105(91)90014-n.
Ribeiro, J.D., 1991b. Effects of surface roughness on the two-dimensional flow past circular cylinders II: fluctuating forces and pressures. J. Wind Eng. Ind. Aerod. 37, 311–326. https://doi.org/10.1016/0167-6105(91)90015-O.
Rocchi, D., Zasso, A., 2002. Vortex shedding from a circular cylinder in a smooth and wired configuration: comparison between 3D LES simulation and experimental analysis. J. Wind Eng. Ind. Aerod. 90, 475–489. https://doi.org/10.1016/S0167-6105(01)00203-3.
Schewe, G., 1983. On the force fluctuations acting on a circular cylinder in crossflow from subcritical up to transcritical Reynolds numbers. J. Fluid Mech. 133, 265–285. https://doi.org/10.1017/s0022112083001913.
Schewe, G., 1986. Sensitivity of transition phenomena to small perturbations in flow round a circular cylinder. J. Fluid Mech. 172, 33–46. https://doi.org/10.1017/S0022112086001635.
Sherif, S.A., Pasumarthi, N., Bartlett, C.S., 1997. A semi-empirical model for heat transfer and ice accretion on aircraft wings in supercooled clouds. Cold Reg. Sci. Technol. 26, 165–179. https://doi.org/10.1016/S0165-232X(97)00021-9.
Shin, J., 1996. Characteristics of surface roughness associated with leading-edge ice accretion. J. Aircraft 33, 316–321. https://doi.org/10.2514/3.46940.
Veerakumar, R., Gao, L., Liu, Y., Hu, H., 2020. Dynamic ice accretion process and its effects on the aerodynamic drag characteristics of a power transmission cable model. Cold Reg. Sci. Technol. 169, 102908. https://doi.org/10.1016/j.coldregions.2019.102908.
Waldman, R.M., Hu, H., 2016. High-speed imaging to quantify transient ice accretion process over an airfoil. J. Aircraft 53, 369–377. https://doi.org/10.2514/1.C033367.
Yamaguchi, H., Nagahawatta, H.D., 1995. Damping effects of cable cross ties in cable-stayed bridges. J. Wind Eng. Ind. Aerod. 54/55, 35–43.
Zdero, R., Turan, O.F., 2010. The effect of surface strands, angle of attack, and ice accretion on the flow field around electrical power cables. J. Wind Eng. Ind. Aerod. 98, 672–678. https://doi.org/10.1016/j.jweia.2010.04.005.
Zdravkovich, M.M., 1981. Review and classification of various aerodynamic and hydrodynamic means for suppressing vortex shedding. J. Wind Eng. Ind. Aerod. 7, 145–189. https://doi.org/10.1016/0167-6105(81)90036-2.
Zuo, D., Jones, N.P., 2010. Interpretation of field observations of wind- and rain-wind-induced stay cable vibrations. J. Wind Eng. Ind. Aerod. 98, 73–87. https://doi.org/10.1016/j.jweia.2009.09.004.